AGU PUBLICATIONS

JGR

Journal of Geophysical Research: Solid Earth

RESEARCH ARTICLE
10.1002/2017JB014876

Key Points:
- The Groningen field shows a clear mechanical stratigraphy in terms of simulated fault gouge friction coefficient and its rate dependence
- The slip stability of anhydrite–carbonate-rich fault rocks is sensitive to pore fluid salinity and sliding velocity
- The top of the Groningen reservoir is most prone to nucleating seismogenic slip from a rate and state friction point of view

Supporting Information:
- Supporting Information S1
- Data Set S1

Correspondence to:
L. B. Hunfeld,
l.b.hunfeld@uu.nl

Citation:
Hunfeld, L. B., Niemeijer, A. R., & Spiers, C. J. (2017). Frictional properties of simulated fault gouges from the seismogenic Groningen gas field under in situ *P–T* -chemical conditions. *Journal of Geophysical Research: Solid Earth*, *122*, 8969–8989. https://doi.org/10.1002/2017JB014876

Received 24 AUG 2017
Accepted 7 NOV 2017
Accepted article online 9 NOV 2017
Published online 27 NOV 2017

Frictional Properties of Simulated Fault Gouges from the Seismogenic Groningen Gas Field Under In Situ *P–T* -Chemical Conditions

L. B. Hunfeld[1], A. R. Niemeijer[1], and C. J. Spiers[1]

[1]HPT Laboratory, Department of Earth Sciences, Utrecht University, Utrecht, The Netherlands

Abstract We investigated the frictional properties of simulated fault gouges derived from the main lithologies present in the seismogenic Groningen gas field (NE Netherlands), employing in situ *P–T* conditions and varying pore fluid salinity. Direct shear experiments were performed on gouges prepared from the Carboniferous shale/siltstone substrate, the Upper Rotliegend Slochteren sandstone reservoir, the overlying Ten Boer claystone, and the Basal Zechstein anhydrite–carbonate caprock, at 100°C, 40 MPa effective normal stress, and sliding velocities of 0.1–10 μm/s. As pore fluids, we used pure water, 0.5–6.2 *M* NaCl solutions, and a 6.9 *M* mixed chloride brine mimicking the formation fluid. Our results show a marked mechanical stratigraphy, with a maximum friction coefficient (μ) of ~0.66 for the Basal Zechstein, a minimum of ~0.37 for the Ten Boer claystone, ~0.6 for the reservoir sandstone, and ~0.5 for the Carboniferous. Mixed gouges showed intermediate μ values. Pore fluid salinity had no effect on frictional strength. Most gouges showed velocity-strengthening behavior, with little systematic effect of pore fluid salinity or sliding velocity on (a–b). However, Basal Zechstein gouge showed velocity weakening at low salinities and/or sliding velocities, as did 50:50 mixtures with sandstone gouge, tested with the 6.9 *M* reservoir brine. From a rate and state friction viewpoint, our results imply that faults incorporating Basal Zechstein anhydrite–carbonate material at the top of the reservoir are the most prone to accelerating slip, that is, have the highest seismogenic potential. The results are equally relevant to other Rotliegend fields in the Netherlands and N. Sea region and to similar sequences globally.

1. Introduction

Faults encountered in boreholes or exposed at the surface by uplift and erosion typically display a fault core where displacement is localized within one or more narrow principal slip zones filled with fine-grained wear material, called fault gouge, derived from the formations that are cut by the fault (Chester & Chester, 1998; Collettini et al., 2009; Sibson, 1986; Toy et al., 2015). The mechanical stability of such faults, that is, whether they accommodate slip via seismic rupture or stable (aseismic) slip, is controlled by the reactivation and subsequent frictional slip behavior of the constituent fault gouge. Experimental studies of the mechanical behavior of fault gouges play a key role in elucidating the mechanics of fault motion and associated earthquake activity in a wide range of geologic settings. Understanding the frictional behavior of fault gouges derived from sedimentary sequences is of key importance to improving our understanding of natural seismicity and seismic hazards in the upper crust (e.g., Collettini et al., 2009; Mizoguchi et al., 2008). It is also becoming crucial to improving our understanding of induced seismicity and associated risks related to hydrocarbons production (e.g., Grasso, 1992; Suckale, 2010), geothermal energy production (e.g., Eberhart-phillips & Oppenheimer, 1984; Majer et al., 2007), wastewater disposal in depleted reservoirs (e.g., Ellsworth, 2013; Elsworth et al., 2016), fluid injection for shale gas production (e.g., Clarke et al., 2014), and to geological storage of CO_2 (e.g., Nicol et al., 2011), natural gas, and hydrogen fuel.

In recent decades, an increasing amount of data has become available from laboratory studies focusing on the frictional properties of natural fault rocks, or their simulated (crushed and sieved) equivalents, sampled from seismically active upper crustal terrains across the globe (Carpenter et al., 2011, 2016; Chen et al., 2015; Collettini et al., 2011; Ikari et al., 2016; Niemeijer & Collettini, 2014; Scuderi et al., 2013; Tembe et al., 2006; Verberne et al., 2010; Zhang & He, 2013) and from hydrocarbon reservoir systems being considered for geological storage of CO_2 (Pluymakers et al., 2014; Samuelson & Spiers, 2012). These studies have shown that the frictional strength of such fault rocks and its slip rate dependence, hence potential for velocity weakening or unstable seismogenic slip in the rate and state friction (RSF) approach to fault mechanics

(Dieterich, 1978, 1979; Marone, 1998; Ruina, 1983; Scholz, 1998, 2002), primarily depend on fault rock composition and true, in situ (pore) pressure and temperature conditions.

One aspect that has not received much attention in the literature on fault friction to date is the possible effect of pore fluid chemistry, through factors such as salinity and pH, on the frictional strength and rate dependence of friction, despite their clear impact on fracture and creep phenomena (Atkinson, 1984; Dove, 1995; Liteanu & Spiers, 2009; Rice, 1978). Pore fluid chemistry may be especially relevant to the mechanical behavior of faults cross-cutting sedimentary sequences, as formation fluids in sedimentary rocks show a wide range of salinities from fresh meteoric waters to brines with salinities exceeding 600 g L^{-1} total dissolved solids (TDS; e.g., Case, 1945; Gledhill & Morse, 2006; Lüders et al., 2010). To our knowledge, studies that address the effects of pore fluid chemistry on friction of granular fault rocks relevant to the shallow upper crust are scarce. Feucht and Logan (1990) observed that frictional strength of precut sandstone rocks (without gouge present initially) can vary with pore fluid ionic strength, presumably due to the effects of the chemically active pore fluids on processes that influence surface roughness and gouge production during sliding. Tullis (1993) investigated the effect of pore fluid pH on the frictional behavior of pure quartz gouges in a limited number of experiments. Significant effects on the time-dependent "evolution effect" of sliding friction (Marone, 1998) were observed, although interpretation of the data remained difficult. Lockner et al. (2006) studied the frictional properties of montmorillonite gouges in the presence of different brines. They observed a systematic increase in frictional strength with increasing pore fluid salinity and attributed their findings to effects of dissolved salts on the properties of fluid layers adsorbed to the clay surfaces (see also Moore & Lockner, 2007). Similar effects of pore fluid chemistry on the residual strength of clays and clay-bearing soils have been reported in the soil mechanics literature (Anson & Hawkins, 1998; Kennely, 1967; Miao & Fenellif, 1994; R. Moore, 1991).

These experimental studies clearly demonstrate that pore fluid chemistry may influence the frictional behavior of fault rocks. However, their applicability to naturally occurring upper crustal fault gouges is limited, as they focused on pure quartz or pure clay gouges only, or, in the case of Feucht and Logan (1990), on bare rock surfaces, and were conducted at room temperature and often at low stress conditions. It is important to investigate to what extent the frictional properties of more realistic gouge compositions are affected by pore fluid chemistry, under conditions that are relevant to their in situ state.

In this contribution, we systematically investigate the roles of pore fluid salinity and fault rock composition on the frictional properties of simulated fault gouges prepared from sedimentary sequences present within the Southern Permian Basin, northwest Europe. Specifically, the formations tested here are Upper Carboniferous and Permian of age and comprise the Rotliegend reservoir and immediate overburden and underlying "underburden" formations that characterize the vast Groningen gas field (Geluk, 2007), located in the northeast of the Netherlands, as well as many other gas fields in the Netherlands and the North Sea (Figure 1). Note here that the Groningen gas field, one of the largest onshore single gas fields in the world, has shown substantial induced seismicity in recent years and that data on fault rock behavior under in situ pressure, temperature, and chemical conditions are urgently needed for assessing seismic hazard (van Thienen-Visser & Breunese, 2015; Van Eijs et al., 2006; Van Wees et al., 2014). The formations investigated were (1) the Carboniferous shales underburden, (2) the Upper Rotliegend Slochteren sandstone reservoir rocks, (3) the overlying Ten Boer claystone, and (4) the Basal Zechstein anhydrite–carbonate caprock. A series of dynamic friction experiments was performed on simulated fault gouges prepared from core and drill cuttings retrieved from these lithologies, at 100°C, 15 MPa pore fluid pressure, and 40 MPa effective normal stress, investigating the frictional strength and rate dependence of friction at imposed sliding rates of 0.1–10 μm/s relevant to earthquake nucleation (Scholz, 2002; Segall & Rice, 2006). In addition to testing the end-member compositions derived from the key formations present in the Groningen field, we also tested mixtures between end-members to simulate gouge smear effects (Lindsay et al., 1992; Yielding et al., 1997). Experiments were performed using pore fluids varying in salinity from deionized water to 4.4 *M* NaCl solution (for the end-member lithologies only), as well as using simulated Groningen reservoir brine (for both end-member lithologies and mixtures), which, besides including high concentrations of NaCl, also includes substantial concentrations of $CaCl_2$ and $MgCl_2$.

The key aim was to assess the effects of formation fluid chemistry and fault rock composition on the potential for induced seismicity in the Groningen gas field and related hydrocarbon reservoirs at depths of ~2–4 km in

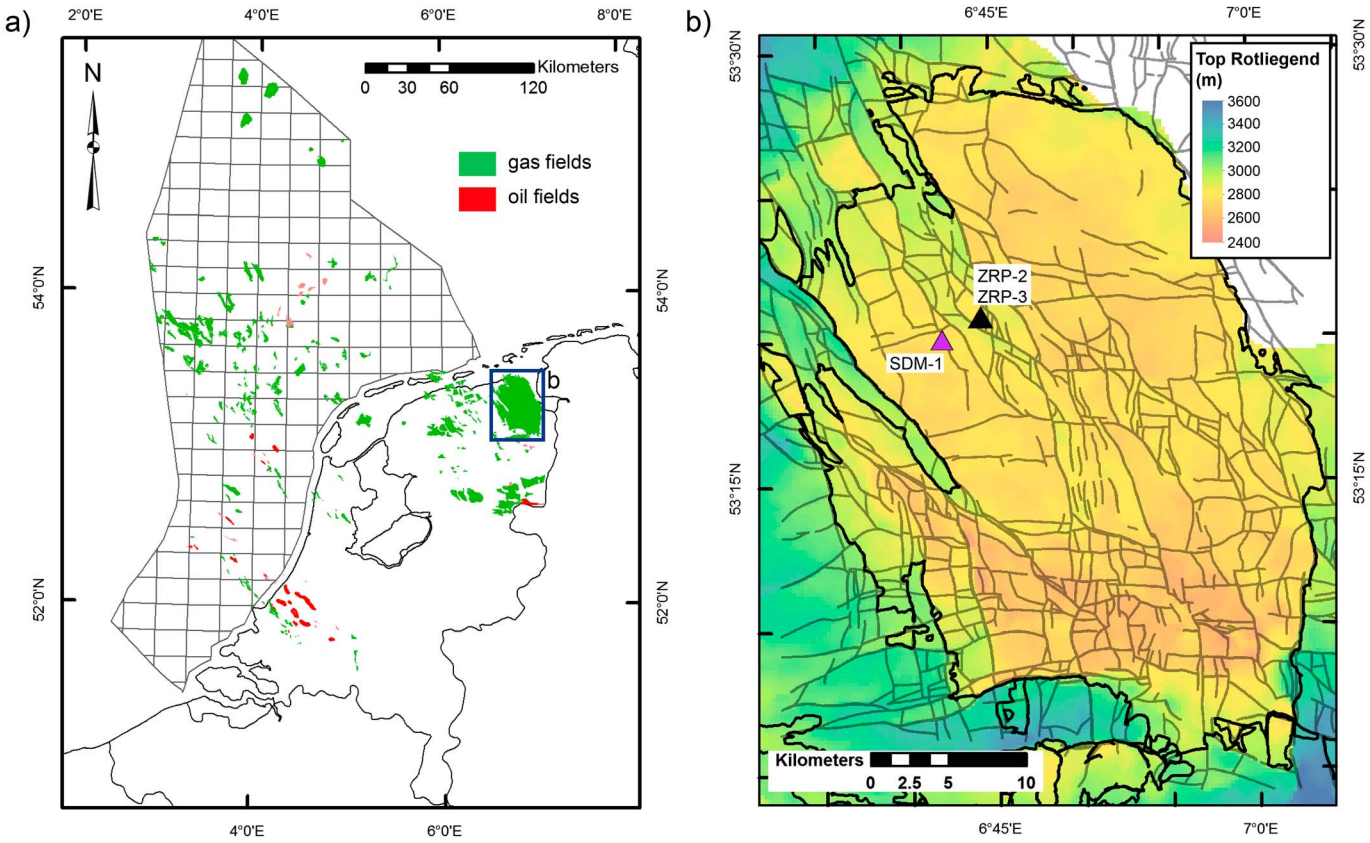

Figure 1. (a) Schematic map of gas and oil fields in the Netherlands and North Sea area. (b) Detailed map of the Groningen gas field, showing the locations of the SDM-1, ZRP-2, and ZRP-3 wells, as well as major faults present in the reservoir (gray lines).

the Netherlands and North Sea basin. However, the relevance of this study is not limited to this setting only. The results are relevant for faults cutting any sedimentary rocks of similar composition and as such have important implications for understanding the effects of pore fluid chemistry on tectonically active faults and induced seismicity in upper crustal sequences globally.

2. Materials and Methods

2.1. Sample Material and Pore Fluids

We obtained sample materials from the Groningen gas field, courtesy of the field operator, the Nederlandse Aardolie Maatschappij BV (NAM). The gas in the Groningen field resides at roughly 3 km depth in Upper Rotliegend reservoir rocks (Slochteren sandstone, thickness 150–200 m), in which it is trapped by a top seal sequence consisting of the Ten Boer claystone (thickness 0–50 m), the Basal Zechstein anhydrite–carbonate caprock (thickness ~50 m), and overlying Zechstein salt (thickness 600–1,000 m; Geluk, 2007). The reservoir rests unconformably on Upper Carboniferous organic-rich shales, siltstones, and coals, which constitute the source rocks for the gas. Core from the Stedum 1 (SDM-1) well and drill cuttings from the Zeerijp 2 (ZRP-2) well, located some 5 km apart in the northern part of the Groningen gas field (see Figure 1), were selected for this study. Figure 2 gives a schematic stratigraphic column of the field, after Geluk (2007), including the depth intervals sampled in the two wells. Samples of the Ten Boer claystone, the Slochteren sandstone, and Carboniferous underburden (henceforth referred to as Carboniferous shale) were selected from the SDM-1 core. Note that the Slochteren sandstone was sampled both above and below the gas–water contact (GWC), located at an absolute depth of ~2,980 m below the surface. Drill cuttings from the Basal Zechstein caprock were obtained from the ZRP-2 well. The part of the reservoir penetrated by the ZRP-2 well lies at a slightly greater absolute depth (see Figure 1), which explains why samples taken from the stratigraphically highest Basal Zechstein caprock come from a greater absolute depth than the stratigraphically lower formations sampled from the SDM-1 core. Samples from each lithology were hand-crushed with

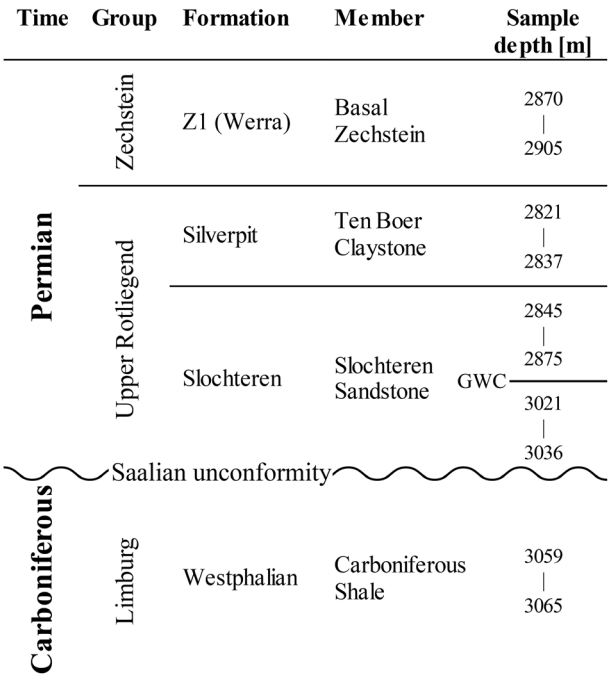

Figure 2. Schematic stratigraphic column showing the reservoir and immediate over- and underburden formations of the Groningen gas field, after Geluk (2007). Samples from the Basal Zechstein were selected from the ZRP-2 well, and samples from the Ten Boer claystone, Slochteren sandstone (both above and below the gas–water contact, denoted with GWC), and Carboniferous shale were selected from the SDM-1 well. The values for sample depth listed are along borehole depths.

pestle and mortar and sieved to a grain size <50 μm, in an effort to simulate the fine-grained gouge material present in the principal slip zones of typical natural fault zones (Chester & Chester, 1998; Sibson, 1986). We also created 50:50 mixtures by weight percent (wt%) between the Basal Zechstein and Ten Boer, the Ten Boer and Slochteren, and the Slochteren and Carboniferous gouges, as well as 25:75, 50:50, and 75:25 mixtures between the Basal Zechstein and Slochteren sandstone. Note that for all mixtures with Slochteren sandstone, we used sandstone samples from above the GWC.

X-ray diffraction (XRD) analysis was performed on all five of the powdered end-member materials (Table 1). Because these analyses yielded semiquantitative compositional data with errors of at least ±5%, we focus on the qualitative differences in composition, reporting major (>10 wt%) and minor constituents (<10 wt%). The Basal Zechstein caprock is a mixture of anhydrite (48%), carbonates (32% calcite and dolomite), and barite (14%), with minor quartz. The Ten Boer claystone is composed predominantly of quartz (48%) and phyllosilicates (39% in total, with 33% muscovite/phengite and 6% chlorite), with minor feldspar, dolomite, and hematite. Both types of Slochteren sandstone showed broadly similar mineralogy, with quartz being the dominant phase. Samples from below the GWC are richer in quartz (83% below versus 67% above) but have only minor feldspar (4%), whereas samples from above the GWC have major feldspar content (19%). Both materials contain minor amounts of clay (kaolinite and phengite) and carbonates. Minor amounts of pyroxene (above GWC) and lazurite (below GWC) are also present, listed as "other" in Table 1. Lastly, the Carboniferous shale is a mixture of quartz (55%), phyllosilicates (35% in total, with 21% illite/chlorite and 14% muscovite/phengite), and feldspar (10%). The compositions of our powdered samples reported here are very similar to the results of compositional analyses of SDM-1 core material reported by Clelland et al. (1987), indicating that they are good representatives of the main lithologies present.

All experiments reported here were performed on samples saturated with pore fluid. Each of the end-member lithologies was tested with the following pore fluids, increasing in salinity: (1) deionized water, (2) 0.5 *M* NaCl solution, (3) 4.4 *M* NaCl solution, and (4) a brine containing 3.4 *M* NaCl, 1.0 *M* $CaCl_2$, 0.1 *M* $MgCl_2$, and minor amounts (<0.1 *M*) of KCl, $SrCl_2$, Na_2SO_4, and $BaCl_2$ (see Table 2). The total ionic strength of this last brine was 6.9 *M* (~10 times the ionic strength of seawater), with ~380 g/L TDS. This brine mimics the exact composition of the formation water sampled from a well close to the ZRP-2 well (namely ZRP-3, see Figure 1) in the Groningen gas field and is believed to be representative for the formation water present in the entire field (NAM, personal communication). In addition, the Basal Zechstein was tested using a 6.2 *M* NaCl solution to simulate the NaCl-saturated fluid likely to exist directly beneath the Zechstein Salt. The mixtures between the end-member lithologies were tested with the 6.9 *M* reservoir brine only. All experiments were performed at 100°C sample temperature (T), using a confining pressure (P_c) of 55 MPa and pore fluid pressure (P_f) of 15 MPa, to approximate the in situ conditions of the Groningen gas reservoir at ~3 km depth (NAM, 2013). Table 3 gives a complete overview of all experiments performed, listing the pore fluids and experimental conditions employed.

Table 1
XRD Data for the Simulated Fault Gouges Used in This Study[a]

Mineral	Basal Zechstein	Ten Boer claystone	Slochteren sandstone (above/below GWC)[b]	Carboniferous shale
Quartz	6	48	67/83	55
Feldspar	—	7	19/4	10
Phyllosilicates	—	39	3/6	35
Carbonates	32	3	6/4	—
Anhydrite	48	—	—/—	—
Barite	14	—	—	—
Hematite	—	2	—/—	—
Other	—	—	5/2	—

[a]The error in the quantitative XRD data reported here is ±5 wt%. [b]GWC denotes gas–water contact.

2.2. Direct Shear Experiments

Direct shear experiments were performed on ~1 mm thick layers of the simulated fault gouges described above using two

Table 2
Reservoir Brine Composition

Salt	Mass concentration (g/L)	Molar concentration (*M*/L)
NaCl	197.7	3.4
$CaCl_2$	147.8	1.0
$MgCl_2$	25.1	0.1
KCl	4.4	6.0×10^{-2}
$SrCl_2$	5.2	2.0×10^{-2}
Na_2SO_4	0.2	6.2×10^{-4}
$BaCl_2$	0.01	4.1×10^{-5}

Note. Total dissolved solid (TDS): ~380 g/L. Total ionic strength: 6.9 *M*.

conventional triaxial testing machines, equipped with a specially designed direct shear assembly (see supporting information, sections S1 and S2; Figure S1). These triaxial machines will be referred to here as the Heard apparatus (Hangx et al., 2010; Peach & Spiers, 1996) and the Shuttle apparatus (Verberne et al., 2013). Differences between these testing machines are minor in practice and have previously been shown not to influence the results of direct shear friction experiments (Pluymakers et al., 2014). Both machines are heated, constant volume triaxial pressure vessels, with silicon oil as the confining medium. In the Heard apparatus, load is transmitted to the sample using a yoke/piston assembly, which is driven by a motor/gearbox/ball-screw system. The Shuttle vessel is loaded by means of an Instron 1362 electro-servo-controlled loading frame. In our experiments, shear stress is imposed on the gouge layer by advancement of the loading piston in the Heard/Shuttle systems, and sliding is initiated at a constant sliding velocity (V) of 5.4 μm/s. To investigate the velocity-dependence of friction of our simulated fault gouges, a velocity-stepping sequence is imposed by varying the displacement rates between 0.1, 1, and 10 μm/s (for the Heard apparatus, these were

Table 3
List of Experiments, Conditions, and Key Mechanical Data

Experiment	Testing machine (H/S)	T (°C)	P_c (MPa)	P_f (MPa)	Pore fluid	μ_{ss} (−)	D_{tot} (mm)	V dependence
Basal Zechstein (BZ)								
Z2BZ-03	H	100	55	15	DI-water	0.641	5.59	Vw/Vs
Z2BZ-01	H	100	55	15	0.5 *M* NaCl	0.658	5.64	Vs
Z2BZ-02	S	100	55	15	0.5 *M* NaCl	0.655	5.54	Vw/Vs
Z2BZ-06	S	100	55	15	4.4 *M* NaCl	0.637	5.50	Vs
Z2BZ-09	S	100	55	15	6.2 *M* NaCl	0.633	5.47	Vs
Z2BZ-24	H	100	55	15	6.9 *M* brine[a]	0.626	5.77	Vs
Ten Boer claystone (TB)								
S1TB-02	H	100	55	15	DI-water	0.362	5.71	Vs
S1TB-01	H	100	55	15	0.5 *M* NaCl	0.380	5.70	Vs
S1TB-03	H	100	55	15	4.4 *M* NaCl	0.378	5.80	Vs
S1TB-08	H	100	55	15	6.9 *M* brine	0.370	5.72	Vs
S1TB-09	H	100	55	15	6.9 *M* brine	0.353	5.71	Vs
Slochteren sandstone (SS) above GWC								
S1SSG-02	H	100	55	15	DI-water	0.608	5.49	Vs
S1SSG-01	H	100	55	15	0.5 *M* NaCl	0.606	5.05	Vs
S1SSG-03	H	100	55	15	4.4 *M* NaCl	0.602	5.45	Vs
S1SSG-06	H	100	55	15	6.9 *M* brine	0.599	5.74	Vs
S1SSG-07	H	100	55	15	6.9 *M* brine	0.619	5.90	Vs
Slochteren sandstone (SS) below GWC								
S1SSW-02	H	100	55	15	DI-water	0.593	5.46	Vs
S1SSW-01	H	100	55	15	0.5 *M* NaCl	0.611	5.94	Vs
S1SSW-03	H	100	55	15	4.4 *M* NaCl	0.594	5.53	Vs
Carboniferous shale (C)								
S1C-02	S	100	55	15	DI-water	0.500	5.52	Vs
S1C-01	H	100	55	15	0.5 *M* NaCl	0.497	5.63	Vs
S1C-03	S	100	55	15	4.4 *M* NaCl	0.494	5.52	Vs
S1C-04	H	100	55	15	6.9 *M* brine	0.498	5.88	Vs
Mixed gouge compositions[b]								
75:25 BZ-SS	H	100	55	15	6.9 *M* brine	0.613	5.79	Vs
50:50 BZ-SS	H	100	55	15	6.9 *M* brine	0.625	5.81	Vw
25:75 BZ-SS	H	100	55	15	6.9 *M* brine	0.613	5.87	Vs
50:50 BZ-TB	H	100	55	15	6.9 *M* brine	0.502	5.85	Vs
50:50 TB-SS	H	100	55	15	6.9 *M* brine	0.517	5.85	Vs
50:50 SS-C	H	100	55	15	6.9 *M* brine	0.610	5.73	Vs

Note. Symbols: H/S indicates use of the Heard (H) or Shuttle (S) triaxial machine; T = temperature; P_c = confining pressure; P_f = pore fluid pressure; μ_{ss} = steady-state friction coefficient obtained at 1.6–2.0 mm shear displacement and sliding velocities of 5.4 μm/s; D_{tot} = total displacement; Vs indicates velocity-strengthening behavior; and Vw velocity-weakening behavior.
[a]6.9 *M* brine denotes the 6.9 *M* total ionic strength reservoir brine. See Table 2 for details. [b]Gouge mixtures with Slochteren sandstone (SS) material used sandstone from above the gas–water contact (GWC).

equivalent to 0.108, 1.08, and 10.8 μm/s) over displacement intervals of 0.3–0.7 mm. A detailed description of the testing procedure is given in the supporting information (section S3).

During each experiment, data on axial load, piston (axial) displacement, confining pressure, temperature, and pore fluid pressure were obtained at a logging rate of 5–10 Hz (see supporting information, section S4). Shear stress (τ) was computed by dividing the internal axial load by the contact area of the shear surface, which is assumed to be equal to the initial contact area. The apparent coefficient of sliding friction (μ) was determined as the ratio of τ to the effective normal stress (σ_n^{eff}), thus assuming zero cohesion (Byerlee, 1978), with a maximum error of ±0.004. Since P_c is at all times equal to σ_n in the current testing assembly, the effective normal stress, defined as $\sigma_n^{eff} = P_c - P_f$, was equal to 40 MPa in all experiments. The velocity dependence of μ was analyzed using the RSF theory (Dieterich, 1978, 1979; Ruina, 1983) and expressed in terms of the rate sensitivity parameter (a–b) (see supporting information, section S4; Figure S2). In short, a positive (a–b) value indicates an increase in friction coefficient with increased sliding velocity, that is, velocity strengthening behavior, which results in stable fault sliding and is associated with aseismic fault slip. By contrast, a negative (a–b) value indicates a lower friction coefficient upon increased sliding velocity, therefore velocity weakening behavior, which is a prerequisite for unstable, stick–slip behavior associated with earthquake nucleation (Marone, 1998; Scholz, 1998). In addition to obtaining values for (a–b), we also obtained values for the individual RSF parameters a, b, and d_c, as described in the supporting information (section S4). It should be noted that changes in friction coefficient related to steps in sliding velocity are often superimposed onto gradual slip weakening or slip hardening trends (e.g., Blanpied et al., 1998). Slip hardening is often associated with a continuous reduction in grain size through cataclasis, whereas slip weakening is associated with ongoing shear localization (Kanagawa et al., 2000; Niemeijer et al., 2008). In our experimental configuration, however, slip weakening might also be related to a decrease in the load-bearing area of contact with increasing displacement.

After each experiment, the direct shear setup was dismantled, and intact fragments of the sheared gouge layers were recovered. These were flushed with demineralized water to remove the brines and then oven-dried for several days. When dried, these fragments were impregnated using Araldite 2020 epoxy resin. Following curing, sections of the impregnated fragments were polished in an orientation parallel to the shear direction and perpendicular to the shear plane and subsequently sputter-coated with a 5 nm thin layer of platinum. This treatment ensured sufficient conduction to allow for SEM analyses with minimal sample charging. The samples were analyzed using a FEI Helios 650UC FIB-SEM, equipped with a retractable, concentric backscatter detector. The samples investigated were imaged in backscattered electron (BSE) mode, using an acceleration voltage of 5–15 kV.

3. Results

3.1. Mechanical Data

3.1.1. Frictional Strength

Key data are listed in Table 3 along with the experimental conditions. The evolution of μ with displacement is presented in Figure 3a for experiments performed on the end-member materials with deionized water and the 6.9 *M* reservoir brine, and in Figure 3b for the 50:50 mixtures using the 6.9 *M* reservoir brine. Experiments on the end-member compositions with the other pore fluids showed almost identical curves to those shown in Figure 3a. Note that the results for the Slochteren sandstone showed virtually no difference between samples derived from above or below the GWC, and we show only the result from above the GWC in Figure 3a to avoid overlap. The tests shown in Figure 3, and indeed all our experiments, were characterized by a rapid, near-linear increase in frictional strength for the first ~0.5 mm of displacement. This was followed by apparent yield and subsequent hardening to a steady-state frictional strength (μ_{ss}, Table 3), attained at ~1–2 mm displacement. After reaching steady state, most experiments show near-linear displacement weakening superimposed on the changes in frictional strength in response to stepwise changes in sliding velocity throughout the experiments. We plot μ_{ss} for all end-member compositions tested versus pore fluid salinity in terms of ionic strength in Figure 3c and for all materials including mixtures versus total phyllosilicate content in Figure 3d.

The anhydrite-rich samples derived from the Basal Zechstein caprock exhibited the highest frictional strength of all materials ($0.63 \leq \mu_{ss} \leq 0.66$) but also the most pronounced displacement weakening. Over the course of

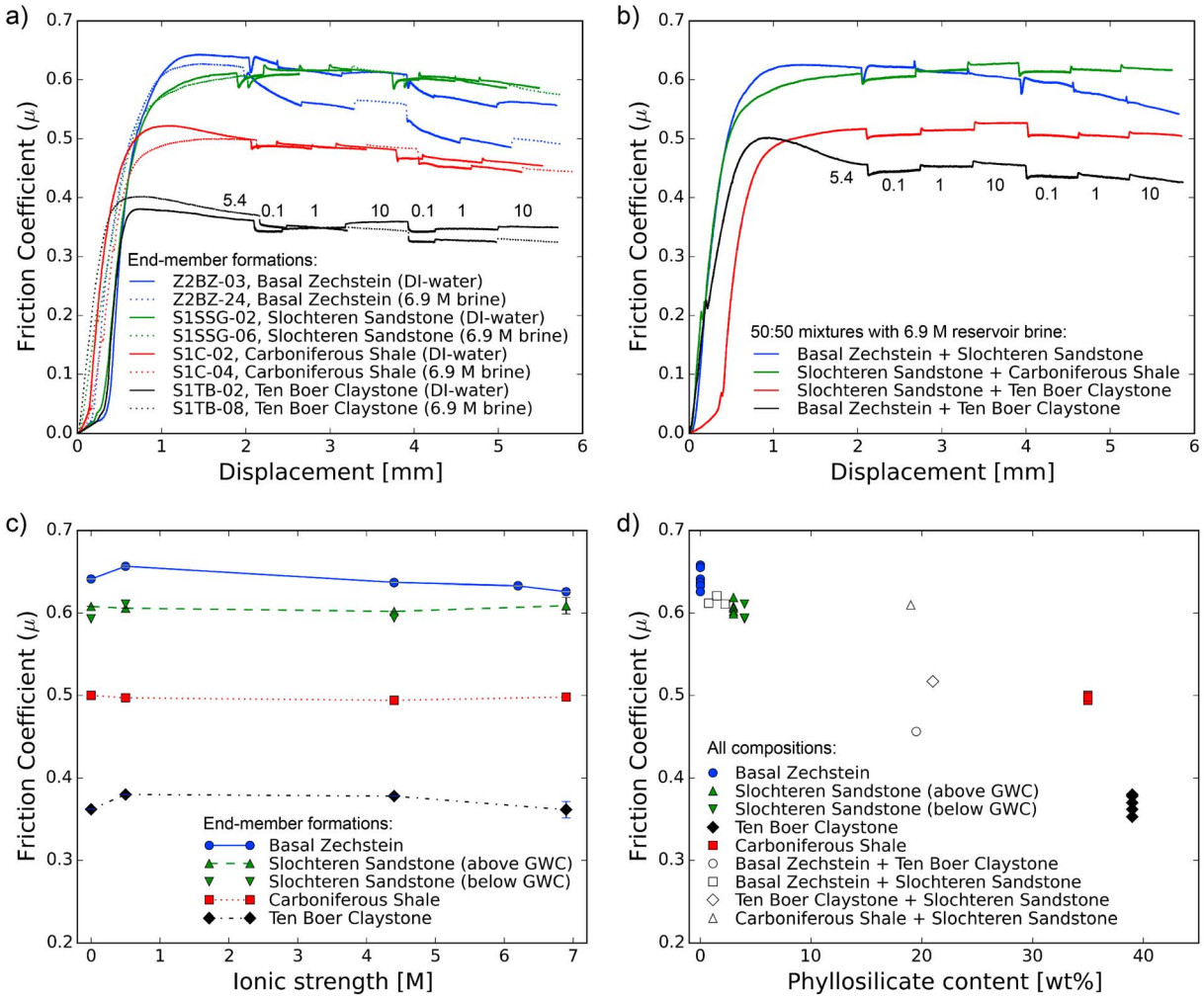

Figure 3. Frictional strength data obtained in this study. (a) Representative friction versus displacement curves for end-member compositions, using deionized water and the 6.9 *M* reservoir brine. (b) Results for 50:50 mixtures using the 6.9 *M* reservoir brine. (c, d) Steady-state friction coefficient obtained at 1.6–2.0 mm displacement (at 5.4 μm/s) (c) versus pore fluid salinity in terms of ionic strength for the end-members and (d) versus total phyllosilicate content for all gouge compositions. The sliding velocities employed are indicated in μm/s next to the friction curves. All experiments were performed at 100°C and 40 MPa σ_n^{eff}.

these experiments, the displacement weakening rate varied slightly (Figure 3a). However, these variations were not systematic with respect to pore fluid salinity. The Slochteren sandstone gouges were slightly weaker, with μ_{ss} values of 0.59–0.62, and showed no systematic difference in strength between samples from above and below the GWC (see Figures 3c and 3d). The lowest frictional strength was observed in the phyllosilicate-rich gouges of the Ten Boer claystone and Carboniferous shale, which display μ_{ss} values of 0.35–0.38 and 0.49–0.50, respectively. The mixed gouges generally showed friction coefficients in between those of their respective end-members (compare Figures 3a and 3b, see also Figure 3d), except for the Slochteren sandstone–Carboniferous shale mixture, which had the same frictional strength as pure Slochteren sandstone gouges. Overall, frictional strength decreased systematically with increased total phyllosilicate content for all gouge compositions, as can be seen in Figure 3d.

The effects of varying pore fluid salinity on frictional strength were small, if present at all (Figure 3c). The Basal Zechstein showed a slightly higher friction coefficient in the presence of 0.5 *M* NaCl ($\mu_{ss} \approx 0.66$), compared to $0.63 \leq \mu_{ss} \leq 0.64$ for the other pore fluids. The Ten Boer claystone showed a similar increase in strength when tested with 0.5 *M* and 4.4 *M* NaCl ($\mu_{ss} \approx 0.38$), compared to deionized water and the 6.9 *M* reservoir brine ($\mu_{ss} \approx 0.36$). The frictional strength of the Slochteren sandstone and Carboniferous shale was unaffected over the full range of salinities tested. The small variations in μ_{ss} observed between samples of the same formation but with different pore fluid salinities were of the same order as the sample variability ($d\mu_{ss} < 0.02$) as

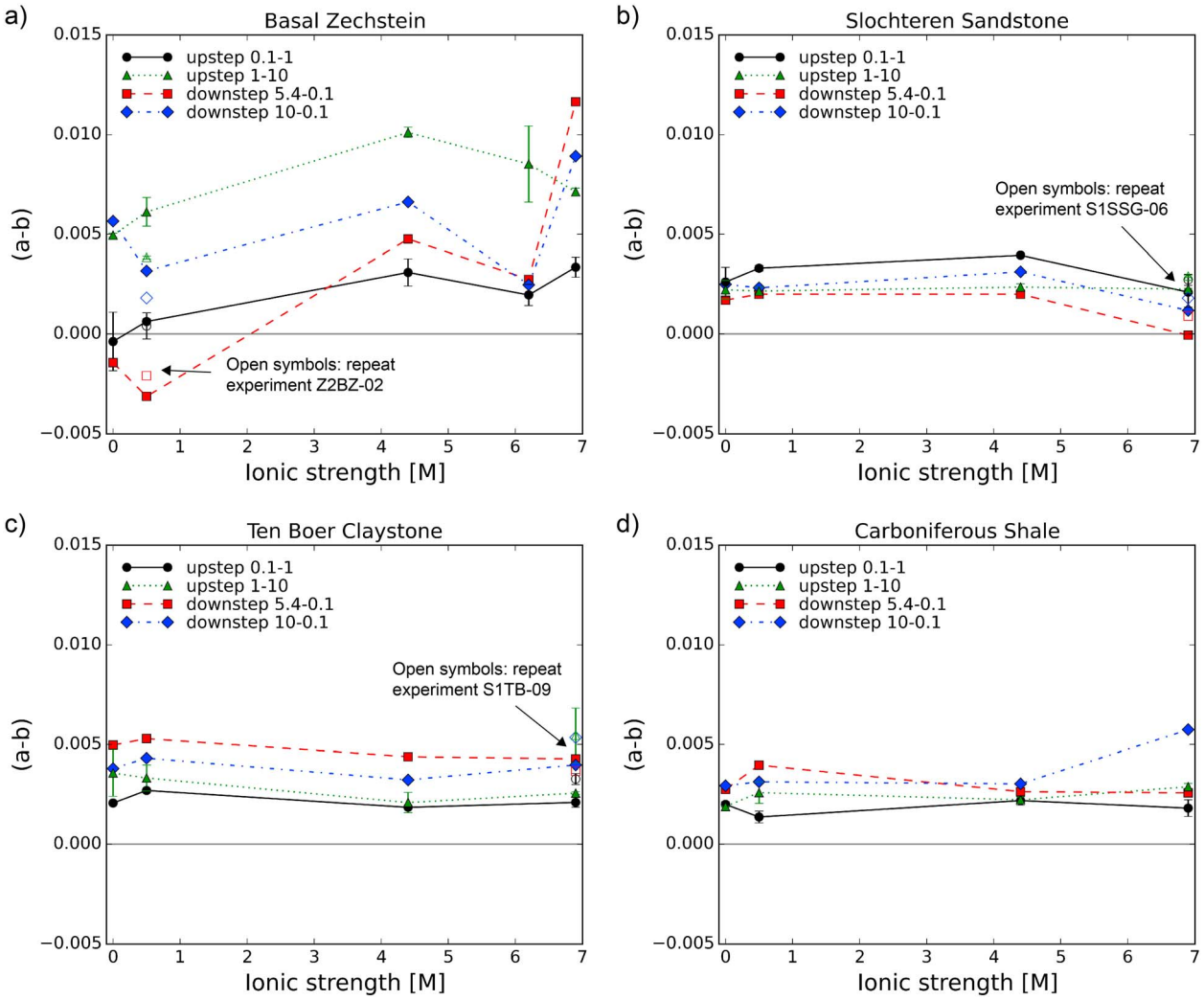

Figure 4. Rate sensitivity parameter (*a*–*b*) plotted against pore fluid salinity in terms of ionic strength for (a) the Basal Zechstein, (b) Slochteren sandstone above the GWC, (c) Ten Boer claystone, and (d) Carboniferous shale. Note that for velocity upsteps, we plot the average (*a*–*b*) value obtained from repeated velocity steps. The error bars indicate the range of values obtained for these steps. Duplicate experiments on the Basal Zechstein and Slochteren sandstone are included in Figures 4a and 4b, respectively. The maximum error to individual (*a*–*b*) values is ±0.002, which is of the same order as the sample variability/reproducibility.

determined from repeat experiments (see Table 3) on the Basal Zechstein (using 0.5 *M* NaCl solution), Slochteren sandstone, and Ten Boer claystone (using the reservoir brine) and did not show any systematic trend with respect to pore fluid salinity.

3.1.2. Rate-Dependence of Frictional Strength

The rate sensitivity parameter (*a*–*b*), as well as the individual parameters *a*, *b*, and d_c, were determined for all velocity steps in the present experiments. A complete list of the values obtained for these parameters is included in the supporting information (Table S1), for reference purposes. In Figure 4, we plot the rate-dependence of friction expressed via (*a*–*b*), against pore fluid salinity in terms of ionic strength for the end-member lithologies tested. Note that in the case of velocity upsteps, we plot the average value of (*a*–*b*) obtained in our experiments for the same velocity steps (upsteps of 0.1 to 1 and 1 to 10 μm/s are performed twice in each experiment, as described in section S3). All velocity steps in experiments performed on the Slochteren sandstone, Ten Boer claystone, and Carboniferous shale show positive (*a*–*b*) values, generally falling between 0.001 and 0.005, thus exhibiting velocity strengthening behavior (Figures 4b, 4c, and 4d). There was virtually no difference in (*a*–*b*) values between Slochteren sandstone samples from above or below the GWC, and for clarity, we only show the values obtained on those from above the GWC in Figure 4b. The data indicate that systematically increasing the salinity of the pore fluid does not alter the rate dependence of friction for the Slochteren, Ten Boer, and Carboniferous lithologies, except for the Slochteren sandstone

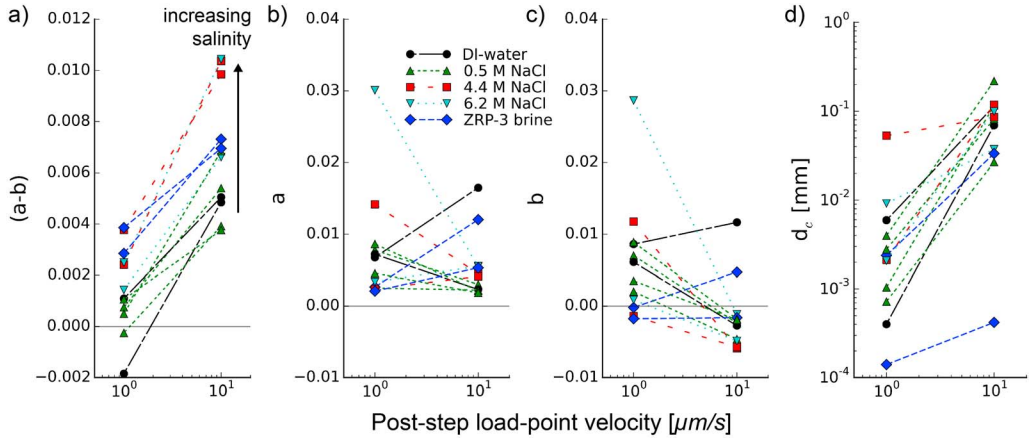

Figure 5. RSF data obtained from experiments on Basal Zechstein gouges. The rate sensitivity parameter (a–b) and the individual parameters a, b, and d_c are plotted versus the poststep load point velocity for all upsteps in sliding velocity. (a–b) increases with increasing velocity in all experiments, irrespective of pore fluid salinity (Figure 5a). Note that experiments with highly saline pore fluids (4.4–6.9 *M*) consistently show higher (a–b) values than when tested with low pore fluid salinity (deionized water-0.5 *M*). The direct effect a does not systematically change with velocity (Figure 5b), in contrast to the evolution effect b, which generally decreases with increased velocity to mostly negative values at 10 μm s^{-1} (Figure 5c). The critical slip distance d_c increases drastically with increased velocity (Figure 5d).

tested in the presence of the 6.9 *M* reservoir brine, which showed slightly lower (a–b). In terms of the individual RSF parameters, the Slochteren, Ten Boer, and Carboniferous derived samples showed no systematic variations in a, b, or d_c with respect to pore fluid salinity, and they have therefore not been plotted separately here. They also showed no consistent trends with respect to sliding velocity, with the exception of a slight positive dependence of (a–b) on sliding velocity observed in most cases for our Ten Boer claystone and Carboniferous shale gouges. For these materials, and for the Slochteren sandstone samples as well, values for a and b are occasionally higher for the faster velocity steps, but not systematically. The phyllosilicate-rich samples derived from the Ten Boer claystone typically showed b values close to zero, or even slightly negative, whereas the Slochteren and Carboniferous derived gouges generally showed positive b values. The critical slip distance d_c for the Slochteren, Ten Boer, and Carboniferous gouges generally fell in the range of 0.002–0.06 mm. For further details, the reader is referred to Table S1 in the supporting information.

The basal Zechstein-derived fault gouges showed markedly different behavior from the other lithologies in terms of rate-dependence of friction (a–b). Our data show that (a–b) for this material is influenced by two factors: (1) pore fluid salinity and (2) sliding velocity. The first effect is shown in Figure 4a. In the presence of low-salinity pore fluids (deionized water or 0.5 *M* NaCl solution), (a–b) values range from −0.003 to +0.006, thus showing both velocity weakening and velocity strengthening behavior. However, when saturated with highly saline pore fluids (4.4–6.9 *M* ionic strength), (a–b) values for the Basal Zechstein gouges are higher, ranging from 0.0013 to 0.012, thus exhibiting solely velocity strengthening behavior. The second effect is shown in Figure 5, where we plot (a–b) and the individual RSF parameters versus the post-step load point velocity, for all upsteps in our experiments on Basal Zechstein gouges. Here (a–b) clearly shows a positive dependence on sliding velocity and much higher values for velocity steps of 1 to 10 μm/s compared to steps of 0.1 to 1 μm/s. This effect is independent of pore fluid salinity, as further highlighted in Figure 5a, where (a–b) values from experiments at low pore fluid salinities are systematically lower than those obtained at high pore fluid salinities. The direct effect a for our Basal Zechstein samples on average does not change significantly over the range of velocities tested, whereas the evolution effect b generally decreases with increasing velocity, shifting to mostly negative values for velocity steps of 1 to 10 μm/s. In addition, the critical slip distance d_c typically shows much higher values for the fast velocity steps (Figure 5d).

In Figure 6, we compare the results in terms of (a–b) from our mixed lithologies with their respective end-members (all tested with the 6.9 *M* reservoir brine). In the case of the Basal Zechstein–Ten Boer mixture, (a–b) values are closely similar to those from the pure Ten Boer sample (Figure 6a), whereas the Ten Boer–Slochteren sandstone mixture showed almost identical (a–b) to the pure Ten Boer claystone (Figure 6c). For the Carboniferous shale–Slochteren sandstone mixture, (a–b) values are intermediate between the two end-members (Figure 6d). In contrast, Basal Zechstein–Slochteren sandstone mixtures

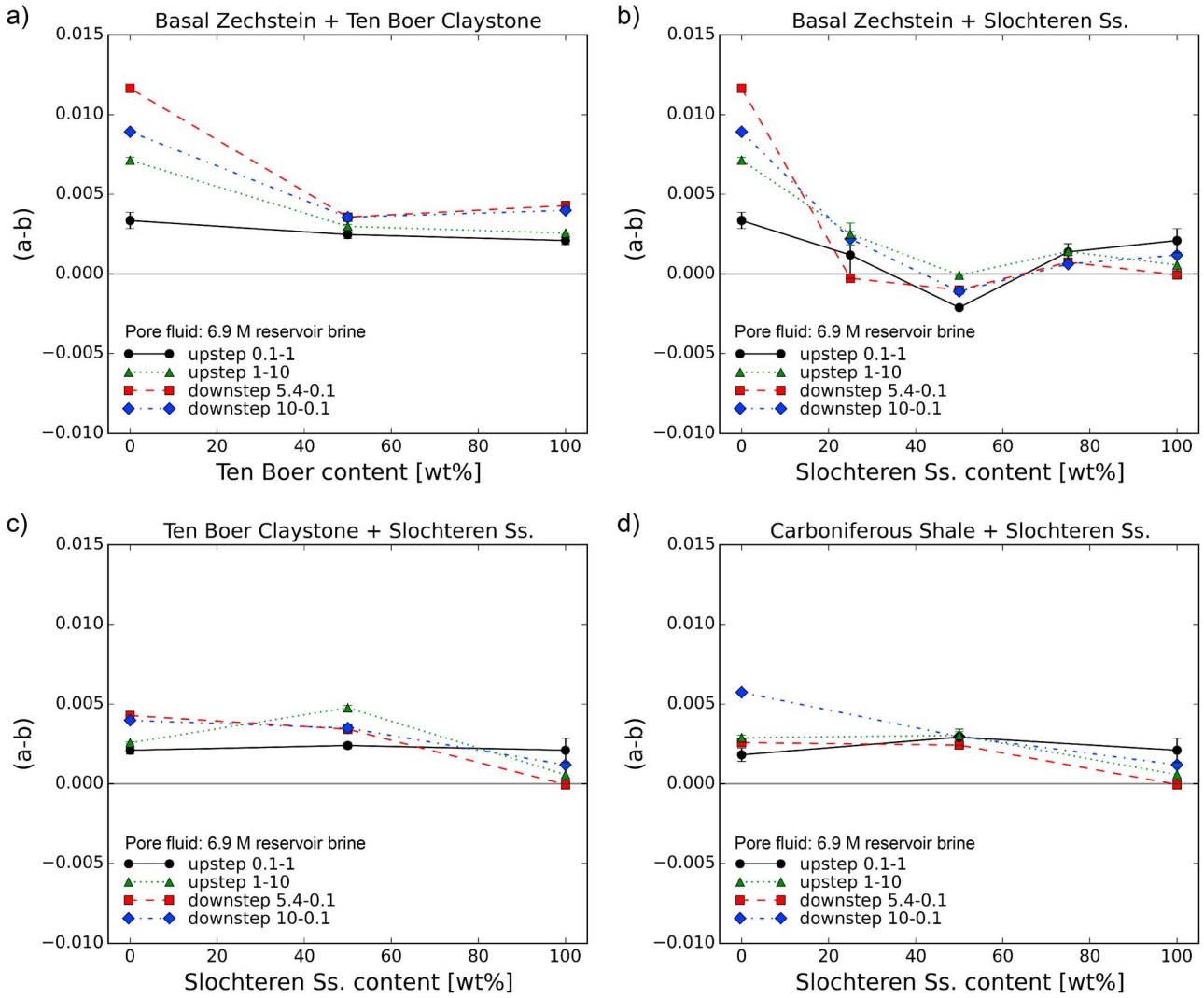

Figure 6. Rate sensitivity parameter (a–b) plotted against either Ten Boer claystone content or Slochteren sandstone content, for all mixed gouge compositions tested. The results for end-member compositions are also included. Note that for velocity upsteps, we plot the average (a–b) value obtained from repeated velocity steps. The error bars indicate the range of values obtained for these steps. The maximum error to individual (a–b) values is ±0.002, which is of the same order as the sample variability/reproducibility.

showed different behavior compared to its end-members (Figure 6b). Here (a–b) shows a V-shaped distribution with respect to sandstone content, with a minimum for the 50:50 mixture. The latter showed velocity weakening behavior for all velocity steps, whereas the pure end-members showed only velocity strengthening behavior. The (a–b) values for the 25:75 and 75:25 Zechstein–Slochteren mixtures fell in between these extremes, showing mostly velocity strengthening slip. Individual a, b, and d_c values for all our mixtures are included in Table S1. In most cases, these were comparable in magnitude to those of the end-member lithologies. In the case of Basal Zechstein–Slochteren sandstone mixtures, however, b values for the 50:50 gouge mixture were generally slightly higher than those for the end-member compositions and other mixture ratios.

Lastly, we focus on the reproducibility of (a–b) and the individual RSF parameters obtained in this study. We performed repeat experiments on the Basal Zechstein (using a 0.5 *M* NaCl solution) and on the Slochteren sandstone and Ten Boer claystone (using the 6.9 *M* reservoir brine), as listed in Table 3. The results for these experiments are included in Figures 4 and 5. In terms of (a–b), our repeat experiments show a maximum absolute difference of <0.002 compared to their duplicates. In addition, our repeat experiments show the same trends in (a–b) with respect to sliding velocity as observed in the other experiments, that is, a positive dependence on sliding velocity in the case of the Basal Zechstein, and no dependence on sliding velocity in

the case of the Slochteren sandstone. For the individual RSF parameters, the maximum absolute difference obtained in these experiments was <0.002 for both a and b, and <0.1 mm for d_c, for both materials. Furthermore, the differences in (a–b) obtained from repeated velocity steps within each individual experiment were of the same order as the reproducibility between experiments and showed no systematic trends with displacement over the full range of sliding velocities tested, for any of the sample materials investigated.

3.2. Microstructures

After the experiments, most of the samples came apart in cohesive fragments, splitting on shear-induced fabrics oriented parallel to the shear direction and close to the sample-forcing block interface, as well as on shear planes in R_1 type Riedel shear orientation (terminology after Logan et al., 1979). Small amounts of sample material typically remained attached to the grooves of the porous plates of the forcing blocks. Therefore, the samples were typically not recovered over their full width, although in some cases the groove imprint was still visible in the sections cut from recovered sample fragments, indicating complete (local) recovery. In Figure 7, we present results of microstructural analyses of sections prepared from our Slochteren sandstone, Ten Boer claystone, Carboniferous shale, and Basal Zechstein samples. No significant differences existed between Slochteren sandstone samples derived from below or above the GWC, and the microstructures shown in Figures 7a–7c are representative for both materials. From experiments on mixed lithologies, we only report the 50:50 Basal Zechstein–Slochteren sandstone sample (shown in Figure 8), as this was the only one that showed clear differences in terms of microstructure (and also rate-dependence of friction, as described above). All samples show evidence for localized deformation on shear bands, but they differ in the type of shear bands and what features define these shear bands, as described below.

The quartz-rich samples of the Slochteren sandstone show a matrix of relatively large (~20–40 μm), subrounded to angular quartz and feldspar grains surrounded by smaller, angular grain fragments, and, locally, clay minerals (Figures 7a–7c). Microfracturing is commonly observed in both quartz and feldspar grains throughout the gouge matrix (see Figure 7b). Grain-to-grain contacts are sharp, with cracks emanating from contact points. Localization occurs in the form of dilatant fractures in the Y shear orientation (Figure 7a), most likely related to postexperiment decompression and unloading. These fractures suggest the presence of Y shears, although we did not observe a clear reduction in grain size toward these fractures nor did we observe preferential grain fracturing within zones surrounding these fractures. In addition to these dilatant fractures, we also observe localization in the form of boundary (B) shears, which are characterized by a reduced grain size with respect to the bulk gouge (Figure 7c). The width of these features is typically at least 40 μm, although a reliable estimate of the total width cannot be made, as most of the samples splitted on B shears and these features were thus not fully preserved. Note that shear bands in the R and P orientation of Logan et al. (1979) were not observed in our Slochteren sandstone samples.

The microstructures of the phyllosilicate-rich Ten Boer claystone samples (Figures 7d–7f) are characterized by a matrix of aligned, anastomosing, very fine-grained clay minerals (from submicron up to a few micron in size) that wrap around subrounded to angular quartz grains ranging in size from ~5 to 50 μm. The aligned clay minerals define a clear foliation in the P and R_1 orientation (Figures 7e and 7f), surrounding quartz grains that in turn show little evidence for grain fracturing and comminution. R_1 and Y shears are abundant, in contrast to P shears, which occurred only sporadically. These shear bands are easily identified, as the samples separated on these shear bands following unloading (Figure 7d). The shear planes tend to wrap around larger quartz grains, rather than cutting straight through them, following horizons of aligned clay particles. The presence of numerous short, dilatant fractures oriented parallel to the shear direction and located near the top of the sample in Figure 7d suggests the presence of a B shear as well. The microstructures of the Carboniferous shale samples (Figures 7g and 7h) were closely similar to those of the Ten Boer claystone, except for the fact that no clear P foliation developed in these samples and that the phyllosilicate content is clearly lower in the Carboniferous gouges compared to the Ten Boer gouges. Microfracturing of quartz and feldspar grains was also more frequently observed in our Carboniferous samples.

In the anhydrite/carbonate-rich samples of the Basal Zechstein (Figures 7i–7k), the matrix consists of mostly angular grains varying in size from ~1 to 50 μm. Grain contacts in the matrix are usually sharp. Carbonate grains, as well as barite and anhydrite grains, are often strongly fractured. Microfracturing can also be observed in quartz grains but is less common. Arrays of fine-grained, strongly comminuted barite (white contrast in Figure 7i) are present in the matrix, often in the vicinity of shear bands, oriented in the P

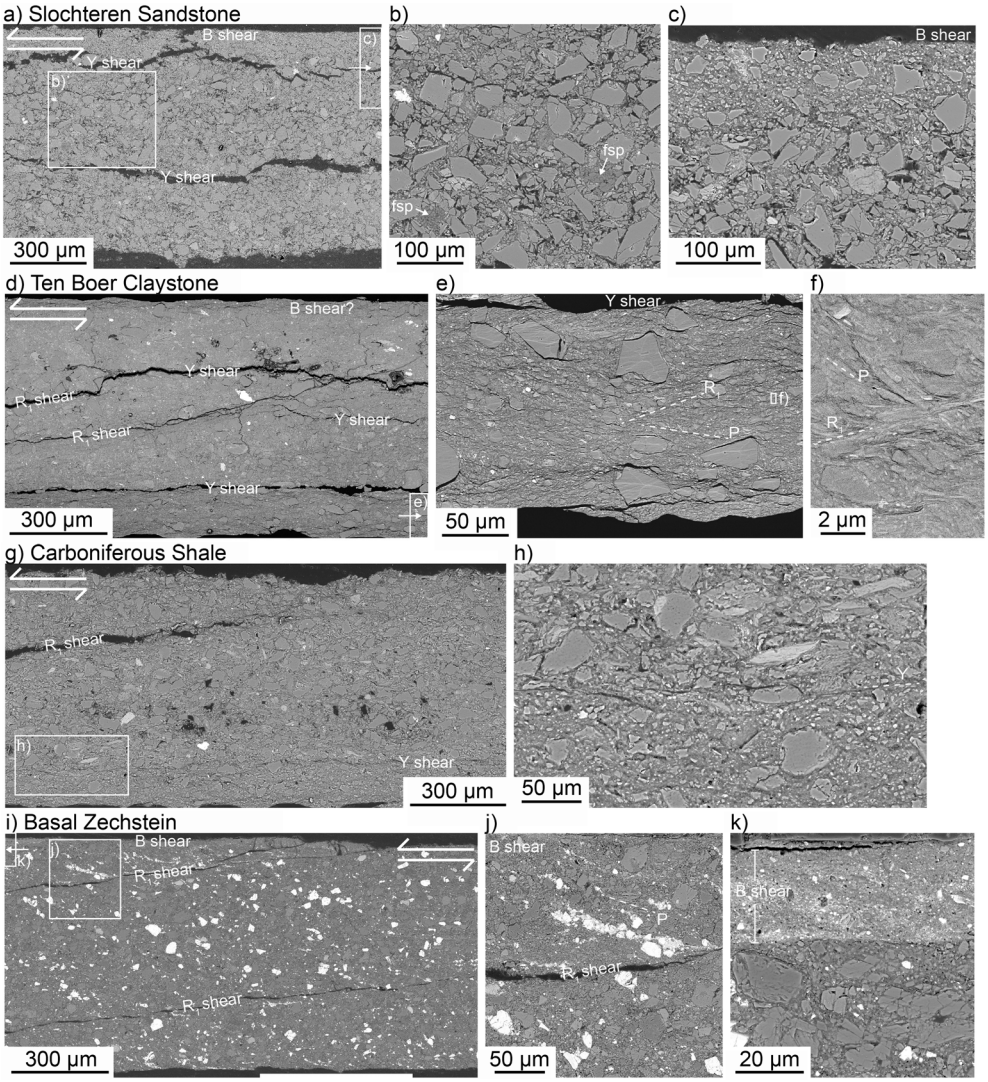

Figure 7. SEM (BSE) micrographs of the end-member compositions. The shear sense in all panels is top to the left. (a) Typical microstructure of Slochteren sandstone gouge (S1SSG-02), showing dilatant fractures in the Y orientation, plus a boundary (B) shear at the top of the micrograph. (b) Part of the gouge bulk in Figure 7a, showing abundant microfracturing. Comminuted feldspar grains are highlighted with arrows marked "fsp." (c) Detail of the B shear in Figure 7a, characterized by a finer grain size compared to the bulk gouge. (d) Typical microstructure of phyllosilicate-rich Ten Boer claystone gouge (S1TB-03). R_1 and Y shears are abundant, often appearing as dilatant fractures, and a B shear may be present at the top of the section. (e) Higher magnification of the bottom right of the same section, showing anastomosing, fine-grained clay minerals wrapping around larger quartz grains, forming R_1 and P foliations. (f) Detail of aligned clay minerals in Figure 7e forming a narrow shear plane in the R_1 orientation. (g) Example of the microstructure exhibited by the Carboniferous shale gouge (S1C-02), showing localization on R_1 and Y shears. (h) Detail of the Y shear in Figure 7g, showing subhorizontal alignment of phyllosilicates. (i) Representative microstructure of Basal Zechstein gouge (Z2BZ-03), showing two R_1 shears and a B shear at the top of the section. (j) Detail of Figure 7i, showing grain size reduction toward R_1 and B shears, and strongly comminuted barite grains (white contrast) in arrays oriented subparallel to the *P* orientation. (k) Detail of the boundary shear in Figure 7i (lighter contrast, pores are black), in which the grain size has been reduced to submicrometer levels.

orientation of Figures 7i and 7j. The dominant shear bands developed in our Basal Zechstein samples are R_1 shears and boundary (B) shears. These are characterized by strong grain size reduction with respect to the bulk gouge material. The R_1 shears are typically very straight, with an occasional step, and propagate through the entire sample from one sample-forcing block interface to the other at an angle of ~10° with respect to the long axis of the sample. B shears, usually at least 25 µm in width, developed close to one or both sample-forcing block interfaces in all experiments. Note that their full width is unknown due to splitting of the samples on B shears. Grain sizes within the core of these B shears have typically been reduced to submicrometer levels (see Figure 7k). The transition from bulk to boundary shear can sometimes be very abrupt, as is the case in Figure 7k, where the boundary shear is characterized by a distinctly brighter grayscale and sudden reduction in grain size.

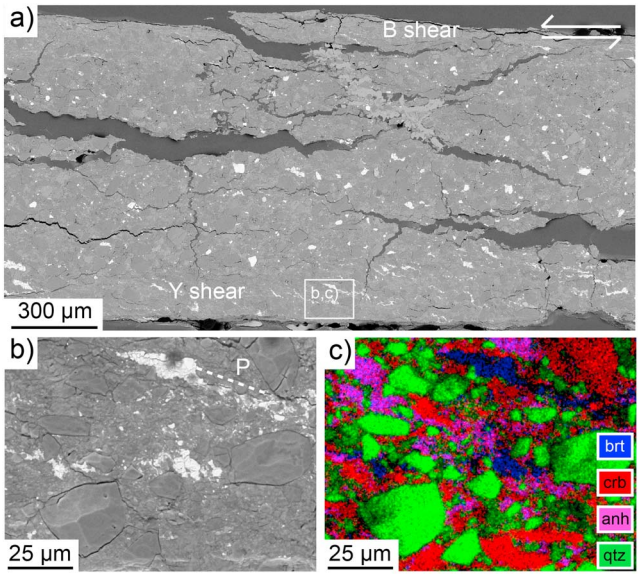

Figure 8. SEM (BSE) micrographs of the 50:50 Basal Zechstein–Slochteren sandstone gouge mixture. The shear sense in all panels is top to the left. (a) Overview of part of the sample recovered, showing abundant dilatant fractures in various orientations, and localization of shear on Y and B shears. (b, c) BSE image and corresponding mineralogical data based on EDX mapping of the location shown in Figure 8a. Relatively large quartz grains (qtz) float in a very fine-grained matrix consisting dominantly of anhydrite (anh), barite (brt), and carbonates (crb). Strongly comminuted barite grains often form arrays in the *P* orientation.

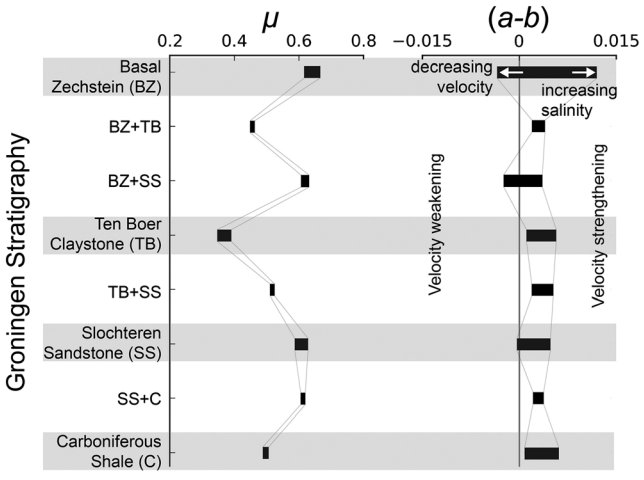

Figure 9. The mechanical stratigraphy of the Groningen gas field in terms of friction coefficient μ and rate sensitivity parameter (a–b). The results for end-member compositions are shown in the gray shaded segments and for mixed gouge compositions in between. Velocity-weakening behavior was only observed for the 50:50 Basal Zechstein–Slochteren sandstone mixture and for Basal Zechstein gouges at the lowest pore fluid salinities and/or sliding velocities investigated. See text for discussion.

Finally, we look at the 50:50 Basal Zechstein–Slochteren sandstone gouge mixture shown in Figure 8. In this sample, the bulk gouge shows a dense matrix consisting dominantly of very fine (1–10 μm) anhydrite, barite, and carbonate grains, with much larger (20–50 μm) clasts, mostly quartz, scattered throughout. The quartz grains in the bulk gouge show little microfracturing. By contrast, the anhydrite, barite, and carbonate grains in the matrix are often fractured. Dilatant fractures in a variety of orientations are common throughout the sample. Localized shear bands, predominantly Y, B, and R_1 shears, were also present. Within these shear bands, the quartz grains typically remain relatively large and undamaged, whereas the grain size of the other minerals has been reduced to submicrometer levels (Figure 8b and 8c). Similar as for the pure Basal Zechstein samples, arrays of strongly comminuted barite grains, often oriented in the P orientation, are also present in the 50:50 Basal Zechstein–Slochteren sandstone mixture.

In summary, the overall microstructural character for the different gouge compositions differed, although localization of deformation on shear bands was observed in all of them. Generally, these localization features appear to be more strongly developed in the Basal Zechstein samples compared to the other lithologies, as grain size reduction is usually much more severe, and the boundaries are usually much more sharply defined by the contrast in grain size. We did not observe any difference in microstructure between samples of the same composition tested with pore fluids of different salinity. This was the case even for samples that showed clear effects of pore fluid salinity on their mechanical behavior (i.e., the rate-dependence of friction for the Basal Zechstein and the steady-state strength of the Ten Boer claystone).

4. Discussion

The present results have shown clear, mineralogy-dependent differences in the frictional properties of the main stratigraphic units present in the Groningen gas field. These are summarized in Figure 9, which shows the mechanical stratigraphy of the field in terms of friction coefficient μ and velocity dependence (a–b). The highest frictional strength was found in the Basal Zechstein caprock ($0.63 \leq \mu_{ss} \leq 0.66$), and the lowest directly underneath, in the Ten Boer claystone ($0.35 \leq \mu_{ss} \leq 0.38$). The Slochteren sandstone reservoir rocks and Carboniferous underburden showed intermediate μ values of ~0.6 and ~0.5, respectively. Mixed gouges showed μ values intermediate between the end-member compositions. All gouge compositions showed velocity strengthening behavior, with little effect of pore fluid salinity on (a–b), except for (1) Basal Zechstein gouges, which showed velocity weakening behavior at the lowest pore fluid salinities and/or sliding velocities investigated, and (2) the 50:50 Basal Zechstein–Slochteren sandstone mixture, which showed velocity weakening behavior at all velocities investigated. In the following, we discuss the influence of mineralogy and pore fluid salinity on fault strength and slip stability for the main stratigraphic units present in the Groningen gas field. We then go on to discuss the implications of our findings in the context of (induced) seismicity in the Groningen field and in sedimentary sequences present in the shallow upper crust in general.

4.1. Influence of Mineralogy on Frictional Strength and Slip Stability

Numerous previous studies (e.g., Byerlee, 1978; Carpenter et al., 2016; Crawford et al., 2008; Giorgetti et al., 2015; Ikari et al., 2007, 2009; Moore & Lockner, 2004, 2011; Takahashi et al., 2007; Tembe et al., 2010) have shown that the frictional strength of fault gouges is strongly influenced by their mineralogy and that especially the presence of abundant phyllosilicate minerals can significantly reduce fault strength, particularly in the presence of water. Our results agree in the sense that frictional strength systematically decreases with increased phyllosilicate content for all gouge compositions tested (Figure 3d). The most phyllosilicate-rich samples, that is, the Ten Boer claystone and the Carboniferous shale, with total phyllosilicate contents of 39 and 35 wt%, respectively (see Table 1), exhibit the lowest frictional strength (μ_{ss} of ~0.36 and ~0.50, respectively, for deionized water-saturated samples; see Figure 3 and Table 3). The quartz-rich Slochteren sandstone, which only contain 3–4 wt% phyllosilicates, and the anhydrite/carbonate-dominated Basal Zechstein, which does not contain detectible phyllosilicates, are significantly stronger (μ_{ss} of ~0.60 and ~0.64, respectively, when saturated with deionized water), in accordance with previous work on quartz-dominated and anhydrite/carbonate-dominated gouges (e.g., Bakker et al., 2016; Pluymakers et al., 2016; Samuelson & Spiers, 2012; Verberne et al., 2010).

The overall decrease in frictional strength with increasing phyllosilicate content observed in experiments where gouge composition is systematically controlled (e.g., Crawford et al., 2008; Moore & Lockner, 2011; Tembe et al., 2010, for quartz–phyllosilicate mixtures and Giorgetti et al., 2015; Ikari et al., 2009, for carbonate–phyllosilicate mixtures) or in gouges of naturally varying composition (e.g., Niemeijer & Vissers, 2014, for quartz–phyllosilicate lithologies & Chen et al., 2015; Niemeijer & Collettini, 2014; Tesei et al., 2012, for carbonate–phyllosilicate lithologies) is typically attributed to a shift in microstructure from a stress-supporting framework of quartz or carbonate grains to a fabric where these relatively competent phases are embedded within a matrix of clay particles, characterized by the development of a relatively planar and pervasive Y foliation or a P foliation and a reduction in Riedel shear angle (Ikari et al., 2011; Moore & Lockner, 2011; Tembe et al., 2010; Tesei et al., 2012). The microstructures of our samples are in good agreement with these models, with the Slochteren sandstone and Basal Zechstein samples showing large quartz or anhydrite/carbonate grains in contact and hence interacting mechanically throughout the bulk of the gouge, with significant microcracking and comminution. By contrast, the Carboniferous shale and Ten Boer claystone show shear localization in aligned phyllosilicate-rich shear bands (Y, B, and R), and, in case of the Ten Boer claystone, the development of a pervasive clay foliation (P). For higher phyllosilicate contents than those tested in the present study, further shear localization within the clay matrix may occur, notably when quartz grains are separated by a critical clay thickness (Tembe et al., 2010), resulting in the low friction coefficients typically reported for gouges with 75 wt% phyllosilicates or more (Crawford et al., 2008; Moore & Lockner, 2011; Tembe et al., 2010). In addition, also the type of phyllosilicate minerals plays a role in determining frictional strength (Moore & Lockner, 2004), possibly contributing to the difference in frictional strength observed in our Ten Boer claystone samples, which contained muscovite/phengite as the dominant phyllosilicate phase, compared to our Carboniferous shale samples, which contained mostly illite/chlorite (see section 2.1).

In contrast to frictional strength, the velocity dependence of friction was not strongly influenced by the presence of phyllosilicates. Samples derived from the Slochteren sandstone, the Ten Boer claystone, and the Carboniferous shale, as well as the 50:50 mixtures, all showed stable velocity-strengthening behavior, with (a–b) values in the range of 0.001–0.005, similar to those reported by Crawford et al. (2008), Tembe et al. (2010), and Moore and Lockner (2011). As for the anhydrite/carbonate-rich samples derived from the Basal Zechstein, we documented (a–b) values in the range of −0.003 to +0.012, comparable to the values reported for simulated anhydrite- or carbonate-dominated gouges under similar conditions (Chen et al., 2015; Pluymakers et al., 2016; Verberne et al., 2010, 2013). However, whether this material exhibited velocity-weakening or velocity-strengthening behavior depended on pore fluid salinity and sliding velocity, which will be discussed in the next section. Additionally, mixing Basal Zechstein gouges with Slochteren sandstone had strong effects on slip stability (Figure 6b). Similar observations were made by Bakker (2017), who tested artificial calcite–quartz mixtures under similar P–T conditions to ours. Velocity-weakening behavior was reported for 50:50 mixtures, whereas the end-members showed velocity-strengthening slip. This behavior was attributed to the contrast in fracture toughness between quartz and calcite, resulting in grain

size reduction preferentially in the weaker phase (calcite), affecting slip stability by influencing the compaction behavior of the gouge. A similar mechanism may have operated in our Basal Zechstein–Slochteren sandstone mixtures, as indeed microfracturing and grain size reduction were observed predominantly in the sulfate and carbonate minerals.

Overall, the agreement between our results and those from the works cited, both in terms of frictional strength and slip stability, suggests that the data obtained in this study are robust and broadly applicable to natural fault zones of similar composition.

4.2. Influence of Pore Fluid Salinity on Frictional Strength and Slip Stability

The results presented in this study show that pore fluid salinity does not significantly influence frictional strength or slip stability of the quartz-rich and phyllosilicate-rich fault gouges tested here. Samples saturated with deionized water show virtually the same friction coefficient and (a–b) values as those saturated with NaCl brines of up to 4.4 M salinity, as well as when saturated with the highly saline reservoir brine (6.9 M ionic strength). In contrast, the anhydrite/carbonate-dominated Basal Zechstein samples did show effects. Although μ values remained unaffected, our velocity-stepping experiments revealed that (a–b) for this material tends to increase with increasing pore fluid salinity and has a positive dependence on sliding velocity. The latter is similar to that seen in previous studies on calcite and anhydrite gouges (Pluymakers et al., 2014; Verberne et al., 2013). In the following, we try to explain these effects. To achieve this, we first briefly discuss the mechanisms controlling the rate dependence of friction in fault rocks of similar composition.

Recent experimental work on fault gouges composed of calcite, anhydrite, and dolomite has shown that these minerals show a transition from stable velocity strengthening to unstable velocity weakening behavior with increasing temperature, occurring at 80–150°C (Chen et al., 2015; Pluymakers et al., 2014, 2016; Scuderi et al., 2013; Verberne, 2015; Verberne et al., 2010, 2013, 2014). This behavior has been attributed to the operation of a thermally activated compaction mechanism, acting alongside dilatant granular flow in the gouge layer, producing velocity-weakening behavior in these materials toward higher temperatures (cf. den Hartog & Spiers, 2014; Niemeijer & Spiers, 2006, 2007). At low temperatures or high sliding velocities, thermally activated compaction is thought to be too slow to significantly influence friction, which is dominated by dilatant granular flow with velocity strengthening friction at sliding grain contacts (Chen & Spiers, 2016; den Hartog & Spiers, 2014). At higher temperatures or low sliding velocities, however, compaction creep within the gouge layer, via water enhanced diffusive mass transfer, is more effective, competing with dilatant granular flow. A steady-state porosity will result from this competition, which will be higher at higher sliding velocity (at constant temperature). A higher porosity implies a lower average contact area and especially contact angle between grains and thus a decrease in friction. This will lead to lower frictional strength at increased sliding velocities and hence velocity weakening behavior (Chen & Spiers, 2016; Niemeijer & Spiers, 2007).

The positive dependence of (a–b) on sliding velocity observed in our Basal Zechstein gouges (Figure 5) is consistent with the above model for the effect of thermally activated compaction. The observed increase in (a–b) in the presence of high salinity pore fluids is more difficult to explain in detail. According to the model, increasing (a–b) values suggest decreasing importance of compaction in the gouge layer. It is not clear, however, why increased pore fluid salinity should slow down compaction by solution transfer processes. An increase in solubility of anhydrite and calcite in the presence of saline solutions is expected to enhance solution transfer (Blounot & Dickson, 1969; Ellis, 1963; Gledhill & Morse, 2006; He & Morse, 1993). On the other hand, the effects of NaCl on the rates of dissolution and precipitation of these minerals may have the opposite effect. The effects of increased salinity on the diffusion coefficient within grain boundary fluids could also affect solution transfer rates.

Data on the effects of NaCl on the kinetics of dissolution/precipitation for minerals like anhydrite, calcite, and dolomite under relevant conditions are scarce, and often conflicting. For calcite, dissolution rates have been reported to increase in the presence of added salts (Gledhill & Morse, 2006), whereas other studies suggest only minor effects (Buhmann & Dreybrodt, 1987; Pokrovsky et al., 2005). The effect of increased ionic strength on the precipitation rates of calcite are also subject to debate (Bischoff, 1968; He & Morse, 1993; Walter, 1986; Zhang & Dawe, 2000; Zuddas & Mucci, 1994). To our knowledge, no

investigations of the effects of high concentrations of NaCl on the diffusion coefficient in grain boundary fluids, and how these affect solution-transfer processes under relevant conditions, exist to date. From compaction experiments on fine-grained, granular calcite aggregates, Liteanu and Spiers (2009) inferred that the presence of 1 *M* NaCl solution slows down compaction by intergranular pressure solution compared to experiments without added salts. The mechanisms responsible, however, remain poorly understood, for the same reasons as stated above. In order to explain our results, new geochemical data are needed on the effects of added salts on these properties under upper crustal pressure and temperature conditions.

4.3. Implications for the Groningen Gas Field

The results presented here for simulated fault gouges derived from the main stratigraphic units present in the Groningen gas field have shown that fault rock composition plays an important role in controlling the frictional behavior of faults cross-cutting the reservoir system. The mechanical stratigraphy shown in Figure 9 shows that the friction coefficient for faults cutting the entire reservoir system can vary strongly, with μ values of ~0.37 for Ten Boer claystone derived gouges, up to ~0.65 in the Basal Zechstein caprock, with values between these two extremes for all other compositions. In terms of seismogenic potential, velocity-weakening behavior was only observed for the 50:50 Basal Zechstein–Slochteren sandstone mixture in the presence of the reservoir brine and in pure Basal Zechstein derived gouges at low salinities (deionized water or 0.5 *M* NaCl) and/or low sliding velocities. At salinities representative for the Groningen reservoir, the latter showed velocity-strengthening behavior. Note however, that independent of salinity, the Basal Zechstein gouges showed a strong positive dependence of (a–b) on sliding velocity (Figure 5), consistent with existing data on pure anhydrite and calcite gouges (Pluymakers et al., 2014; Verberne et al., 2013), and conceptual microphysical model interpretations for the onset of velocity weakening in these materials (Chen & Spiers, 2016; Niemeijer & Spiers, 2007; Verberne et al., 2014). Linear extrapolation of our data in Figure 7a toward lower sliding velocities suggests that even for high salinities, velocity weakening behavior can be expected in Basal Zechstein gouges at sliding velocities one order of magnitude lower than tested here, favoring nucleation of unstable slip. On the other hand, subsequent evolution toward higher slip rates will be accompanied by an increase in (a–b), switching to velocity strengthening behavior, eventually reducing the potential for further acceleration of slip. To validate this and to evaluate whether the velocity effect on (a–b) outweighs the salinity effect observed in the Basal Zechstein material, more experiments are needed over a broader range of sliding velocities. Additionally, the effect of a transition of velocity weakening to velocity strengthening on potential rupture nucleation should be investigated.

From a purely RSF point of view and assuming a uniformly stressed fault, our results imply that the upper part of the reservoir system is most prone to earthquake nucleation, that is, that faults cutting and hence incorporating Basal Zechstein material, or with offsets well in excess of the thickness of the Ten Boer Formation, and so juxtaposing Basal Zechstein directly against Slochteren sandstone and thus creating a mixed gouge, have the highest seismogenic potential. However, little evidence from earthquake hypocenter estimations is available to support this. The most accurate hypocenter estimations of induced earthquakes in Groningen published to date (typically with vertical uncertainty of 100–200 m), by Spetzler and Dost (2017), indicate that induced events occur over the full extent of the reservoir system, although there seems to be a slight tendency for an increased number of events toward the top of the reservoir. It should be noted, however, that the seismic source does not necessarily have to coincide with the point of nucleation (Lapusta & Rice, 2003; see also Kaneko et al., 2016). Additionally, there are other (mechanical) factors that may influence the location of rupture nucleation. For example, a uniform stress distribution is unlikely in the real system. Instead, stress concentrations can be expected locally on faults with sufficient offset where mechanically contrasting layers are juxtaposed (Buijze et al., 2015; Mulders, 2003). Furthermore, the presence of the viscoelastic rocksalt overlying the Basal Zechstein may further influence the state of stress locally, potentially affecting fault reactivation (Orlic & Wassing, 2012; Wassing et al., 2017). The fact that induced events do not seem to be uniquely associated with the top of the reservoir may also be related to other types of mechanical behavior, besides rate-dependent effects. It is known that slip weakening (Ida, 1972; Ikari et al., 2013) is also capable of producing accelerating slip. The potential for this type of behavior needs to be investigated for Groningen fault rocks in future studies.

4.4. Broader Implications

Besides being directly relevant to Groningen, the results presented here are also relevant to other hydrocarbon reservoirs present in the Netherlands and the North Sea (e.g., Buntsandstein reservoirs; De Jager & Geluk, 2007) and to individual lithologies and sequences of similar composition in the upper crust globally. The salinity of formation waters in sedimentary sequences typically varies between 72 g/L TDS for meteoric water to 600 g/L TDS for saline aquifers (Case, 1945; Hanor, 1994). These brines are generally a mixture of salts, containing mostly NaCl, $MgCl_2$, and $CaCl_2$. This is also the case for formation waters of many hydrocarbon reservoirs present in the Southern Permian Basin in northwest Europe (Lüders et al., 2010), including the Groningen gas field. From our experiments on simulated fault gouges from the Groningen field, employing pore fluid salinities up to ~380 g/L TDS, we infer that the presence of these brines has little influence on the frictional strength and slip stability of gouges derived from quartz- and/or phyllosilicate-rich formations similar to the Slochteren sandstone, Ten Boer claystone, or Carboniferous shale/siltstone and hence on fault (re)activation and the potential for (induced) seismicity in such formations.

On the other hand, our results for Basal Zechstein gouges suggest that the rate dependence of friction of fault gouges consisting primarily of sulfate and carbonate minerals such as anhydrite, calcite, and dolomite can be strongly affected by pore fluid salinity. Fluid–rock interactions seem to play a key role here, although the underlying mechanisms for this effect remain poorly understood at this stage. This sensitivity of (a–b) to pore fluid salinity is relevant not only to induced seismicity in hydrocarbon reservoirs that are topped by anhydrite/carbonate sequences, like the Groningen gas field and many other Rotliegend gas fields present in the Southern Permian Basin (Geluk, 2007), but also to natural seismicity in evaporite and limestone terrains, like the Triassic Evaporites of the Burano Formation in the Italian Apennines (Collettini et al., 2008, 2009; De Paola et al., 2008). In such settings, the effects of pore fluid chemistry should be included in the analyses of fault stability. This requires further investigation in the future, as most data on relevant fault rock compositions have been obtained using pure water as a pore fluid.

5. Conclusions

We have performed direct shear, velocity-stepping friction experiments on simulated fault gouges prepared from core and drill cuttings from the main stratigraphic units present in the seismogenic Groningen gas field. Besides employing the in situ P–T conditions (100°C and 40 MPa effective normal stress), we also investigated effects of pore fluid salinity, using pore fluids varying in salinity between deionized water and 4.4 M NaCl, as well as using a 6.9 M ionic strength brine (mainly NaCl, $CaCl_2$, and $MgCl_2$) mimicking the formation water present in the Groningen field. Our aim was to investigate the influence of fault rock composition and pore fluid salinity on the frictional strength and slip stability of fault gouges representative for the Groningen field, as well as for fault rocks derived from similar lithologies in general. Our main findings can be summarized as follows:

1. Our results show a strongly varying mechanical stratigraphy, with a maximum coefficient of friction (μ) of ~0.66 for the Basal Zechstein caprock and minimum of ~0.37 for the Ten Boer claystone. The Slochteren sandstone reservoir and Carboniferous underburden show intermediate μ values of ~0.6 and ~0.5, respectively. Mixed gouges showed μ values between the end-member compositions. Frictional strength decreased systematically with increasing phyllosilicate content but was not sensitive to pore fluid salinity.
2. The microstructures of all sample materials tested showed localization into Riedel shears and boundary shears. Significant grain size reduction was observed in shear bands in Basal Zechstein and Slochteren sandstone gouges, whereas their 50:50 mixture showed preferential grain size reduction in the sulfate and carbonate phases both in the matrix and in the shear bands. The phyllosilicate-bearing gouges showed localized deformation on aligned phyllosilicate horizons. No significant microstructural differences were observed between samples tested with different pore fluid salinities.
3. All gouge compositions showed velocity strengthening behavior, with little effect of pore fluid salinity or sliding velocity on (a–b), except for (i) Basal Zechstein gouges, which showed velocity weakening behavior at the lowest pore fluid salinities and/or sliding velocities investigated, and (ii) the 50:50 Basal Zechstein–Slochteren sandstone gouge mixture tested with the reservoir brine, which showed exclusively velocity weakening slip.

4. Our results imply that faults incorporating Basal Zechstein material, or Basal Zechstein plus Slochteren sandstone, have the highest potential for generating accelerating slip. From a rate and state friction point of view, the upper part of the reservoir system, where faults cut the Basal Zechstein or juxtapose Basal Zechstein against the reservoir sandstone, is thus the most prone to seismogenesis.
5. Based on our findings, we infer that the saline pore fluid conditions that are common in many sedimentary sequences generally will not affect frictional strength and slip stability of faults filled with quartz- and/or phyllosilicate-dominated gouges. By contrast, the slip stability of fault gouges rich in sulfate and carbonate minerals like anhydrite, calcite, and dolomite may be sensitive to pore fluid salinity. This requires further investigation, as most data obtained so far have been for pure water as a pore fluid.

Acknowledgments
This research was funded by the Nederlandse Aardolie Maatschappij BV (NAM), in the framework of the broad research program that the company initiated following the $M_L = 3.6$ Huizinge earthquake in 2012. The technical staff of the HPT Laboratory at Utrecht University are thanked for their assistance, specifically Gert Kastelein, Eimert de Graaff, Floris van Oort, and Peter van Krieken. Otto Stiekema and Leonard Bik are thanked for preparing the sections. We also thank Diane Moore and Matt Ikari for their constructive reviews that helped improve this paper. A. R. Niemeijer is funded by the European Research Council starting grant SEISMIC (335915) and by the Netherlands Organization for Scientific Research (NWO) through VIDI grant 854.12.011. The data for this paper are available as Hunfeld, Luuk; Niemeijer, André; Spiers, Christopher (2017): Friction data of simulated fault gouges derived from the Groningen gas field. GFZ Data Services. http://doi.org/10.5880/fidgeo.2017.014.

References

Anson, R. W. W., & Hawkins, A. B. (1998). The effect of calcium ions in pore water on the residual shear strength of kaolinite and sodium montmorillonite. *Geotechnique*, *48*(6), 787–800. https://doi.org/10.1680/geot.1998.48.6.787

Atkinson, K. (1984). Subcritical crack growth in geological materials. *Journal of Geophysical Research*, *89*(B6), 4077–4114. https://doi.org/10.1029/JB089iB06p04077

Bakker, E. (2017). Frictional and transport properties of simulated faults in CO_2 storage reservoirs and clay-rich caprocks, Ph.D. thesis, Utrecht University.

Bakker, E., Hangx, S. J. T., Niemeijer, A. R., & Spiers, C. J. (2016). Frictional behaviour and transport properties of simulated fault gouges derived from a natural CO_2 reservoir. *International Journal of Greenhouse Gas Control*, *54*, 70–83. https://doi.org/10.1016/j.ijggc.2016.08.029

Bischoff, J. L. (1968). Kinetics of calcite nucleation: Magnesium inhibition and ionic strength catalysis. *Journal of Geophysical Research*, *73*(10), 3315–3322. https://doi.org/10.1029/JB073i010p03315

Blanpied, M. L., Marone, C. J., Lockner, D. A., Byerlee, J. D., & King, D. P. (1998). Quantitative measure of the variation in fault rheology due to fluid–rock interactions. *Journal of Geophysical Research*, *103*(B5), 9691–9712. https://doi.org/10.1029/98JB00162

Blounot, C. W., & Dickson, F. W. (1969). The solubility of anhydrite ($CaSO_4$) in NaCl–H_2O from 100 to 450°C and 1 to 1000 bars. *Geochimica et Cosmochimica Acta*, *33*(2), 227–245. https://doi.org/10.1016/0016-7037(69)90140-9

Buhmann, D., & Dreybrodt, W. (1987). Calcite dissolution kinetics in the system H_2O–CO_2–$CaCO_3$ with participation of foreign ions. *Chemical Geology*, *64*1-2, 89–102. https://doi.org/10.1016/0009-2541(87)90154-9

Buijze, L., Orlic, B., & Wassing, B. B. T. (2015). Modeling of dynamic fault rupture in a depleting gas field, TNO report 2015 R10844.

Byerlee, J. (1978). Friction of rocks. *Pure and Applied Geophysics PAGEOPH*, *116*(4-5), 615–626. https://doi.org/10.1007/BF00876528

Carpenter, B. M., Marone, C., & Saffer, D. M. (2011). Weakness of the San Andreas fault revealed by samples from the active fault zone. *Nature Geoscience*, *4*(4), 251–254. https://doi.org/10.1038/ngeo1089

Carpenter, B. M., Ikari, M. J., & Marone, C. J. (2016). Laboratory observations of time-dependent frictional strengthening and stress relaxation in natural and synthetic fault gouges. *Journal of Geophysical Research: Solid Earth*, *121*, 1183–1201. https://doi.org/10.1002/2015JB012136

Case, L. C. (1945). Exceptional Silurian brine near Bay City, Michigan. *American Association of Petroleum Geologists Bulletin*, *29*, 567–570.

Chen, J., & Spiers, C. J. (2016). Rate and state frictional and healing behavior of carbonate fault gouge explained using microphysical model. *Journal of Geophysical Research: Solid Earth*, *121*, 8642–8665. https://doi.org/10.1002/2016JB013470

Chen, J., Verberne, B. A., & Spiers, C. J. (2015). Effects of healing on the seismic potential of carbonate fault rocks: Experiments on samples from the Longmenshan fault, Sichuan, China. *Journal of Geophysical Research: Solid Earth*, *120*, 5479–5506. https://doi.org/10.1002/2014JB011859.Received

Chester, F. M., & Chester, J. S. (1998). Ultracataclasite structure and friction processes of the Punchbowl fault, San Andreas system, California. *Tectonophysics*, *295*(1-2), 199–221. https://doi.org/10.1016/S0040-1951(98)00121-8

Clarke, H., Eisner, L., Styles, P., & Turner, P. (2014). Felt seismicity associated with shale gas hydraulic fracturing: The first documented example in Europe. *Geophysical Research Letters*, *41*(23), 8308–8314. https://doi.org/10.1002/2014GL062047

Clelland, W. D., Kantorowicz, J. D., Nicholls, C. A., de Weerd, J., & de Gier, F. A. M. (1987). Pilot study into the diagenesis of the northern Groningen wells: Stedum-1, Uithuizermeeden-1 and Delfzijl-1, onshore Netherlands. *Technical Service Report RKTR.87.282*.

Collettini, C., Cardellini, C., Chiodini, G., De Paola, N., Holdsworth, R. E., & Smith, S. A. F. (2008). Fault weakening due to CO2 degassing in the northern Apennines: Short- and long-term processes. *Geological Society of London, Special Publication*, *299*(1), 175–194. https://doi.org/10.1144/SP299.11

Collettini, C., De Paola, N., & Faulkner, D. R. (2009). Insights on the geometry and mechanics of the Umbria-Marche earthquakes (Central Italy) from the integration of field and laboratory data. *Tectonophysics*, *476*(1-2), 99–109. https://doi.org/10.1016/j.tecto.2008.08.013

Collettini, C., Niemeijer, A. R., Viti, C., Smith, S. A. F., & Marone, C. (2011). Fault structure, frictional properties and mixed-mode fault slip behavior. *Earth and Planetary Science Letters*, *311*(3-4), 316–327. https://doi.org/10.1016/j.epsl.2011.09.020

Crawford, B. R., Faulkner, D. R., & Rutter, E. H. (2008). Strength, porosity, and permeability development during hydrostatic and shear loading of synthetic quartz-clay fault gouge. *Journal of Geophysical Research*, *113*, B03207. https://doi.org/10.1029/2006JB004634

De Jager, J., & Geluk, M. C. (2007). Petroleum geology. In *Geology of the Netherlands* (pp. 241–264). Amsterdam: Royal Netherlands Academy of Arts and Sciences.

De Paola, N., Collettini, C., Faulkner, D. R., & Trippetta, F. (2008). Fault zone architecture and deformation processes within evaporitic rocks in the upper crust. *Tectonics*, *27*, TC4017. https://doi.org/10.1029/2007TC002230

den Hartog, S. A. M., & Spiers, C. J. (2014). A microphysical model for fault gouge friction applied to subduction megathrusts. *Journal of Geophysical Research: Solid Earth*, *119*, 1510–1529. https://doi.org/10.1002/2014JB011151.Received

Dieterich, J. H. (1978). Preseismic fault slip and earthquake prediction. *Journal of Geophysical Research*, *83*(B8), 3940. https://doi.org/10.1029/JB083iB08p03940

Dieterich, J. H. (1979). Modeling of rock friction: 1. Experimental results and constitutive equations. *Journal of Geophysical Research*, *84*(B5), 2161–2168. https://doi.org/10.1029/JB084iB05p02161

Dove, P. M. (1995). Geochemical controls on the kinetics of quartz fracture at subcritical tensile stresses. *Journal of Geophysical Research*, *100*(B11), 22,349–22,359. https://doi.org/10.1029/95JB02155

Eberhart-phillips, D., & Oppenheimer, D. H. (1984). Induced seismicity in the Geysers geothermal area, California. *Journal of Geophysical Research*, *89*(B2), 1191–1207. https://doi.org/10.1029/JB089iB02p01191

Ellis, A. J. (1963). The solubility of calcite in sodium chloride solutions at high temperatures. *American Journal of Science*, *261*(3), 259–267. https://doi.org/10.2475/ajs.261.3.259

Ellsworth, W. L. (2013). Injection-induced earthquakes. *Science*, *341*(6142), 1225942. https://doi.org/10.1126/science.1225942

Elsworth, D., Spiers, C. J., & Niemeijer, A. R. (2016). Understanding induced seismicity. *Science*, *354*(6318), 1380–1381. https://doi.org/10.1126/science.aal2584

Feucht, L. J., & Logan, J. M. (1990). Effects of chemically active solutions on shearing behavior of a sandstone. *Tectonophysics*, *175*(1-3), 159–176. https://doi.org/10.1016/0040-1951(90)90136-V

Geluk, M. C. (2007). Permian. In T. E. Wong, D. A. J. Batjes, & J. De Jager (Eds.), *Geology of the Netherlands* (pp. 63–84). Amsterdam: Royal Netherlands Academy of Arts and Sciences.

Giorgetti, C., Carpenter, B. M., & Collettini, C. (2015). Frictional behavior of talc-calcite mixtures. *Journal of Geophysical Research: Solid Earth*, *120*, 6614–6633. https://doi.org/10.1002/2015JB011970

Gledhill, D. K., & Morse, J. W. (2006). Calcite solubility in Na–Ca–Mg–Cl brines. *Chemical Geology*, *233*(3-4), 249–256. https://doi.org/10.1016/j.chemgeo.2006.03.006

Grasso, J. R. (1992). Mechanics of seismic instabilities induced by the recovery of hydrocarbons. *Pure and Applied Geophysics PAGEOPH*, *139*(3-4), 507–534. https://doi.org/10.1007/BF00879949

Hangx, S. J. T., Spiers, C. J., & Peach, C. J. (2010). Mechanical behavior of anhydrite caprock and implications for CO_2 sealing capacity. *Journal of Geophysical Research*, *115*, B07402. https://doi.org/10.1029/2009JB006954

Hanor, J. S. (1994). Origin of saline fluids in sedimentary basins. *Geological Society of London, Special Publication*, *78*(1), 151–174. https://doi.org/10.1144/GSL.SP.1994.078.01.13

He, S., & Morse, J. W. (1993). The carbonic acid system and calcite solubility in aqueous Na–K–Ca–Mg–Cl–SO_4 solutions from 0 to 90°C. *Geochimica et Cosmochimica Acta*, *57*(15), 3533–3554. https://doi.org/10.1016/0016-7037(93)90137-L

Ida, Y. (1972). Cohesive force across the tip of a longitudinal-shear crack and Griffith's specific surface energy. *Journal of Geophysical Research*, *77*(20), 3796–3805. https://doi.org/10.1029/JB077i020p03796

Ikari, M. J., Saffer, D. M., & Marone, C. (2007). Effect of hydration state on the frictional properties of montmorillonite-based fault gouge. *Journal of Geophysical Research*, *112*, B06423. https://doi.org/10.1029/2006JB004748

Ikari, M. J., Saffer, D. M., & Marone, C. (2009). Frictional and hydrologic properties of clay-rich fault gouge. *Journal of Geophysical Research*, *114*, B05409. https://doi.org/10.1029/2008JB006089

Ikari, M. J., Niemeijer, A. R., & Marone, C. (2011). The role of fault zone fabric and lithification state on frictional strength, constitutive behavior, and deformation microstructure. *Journal of Geophysical Research*, *116*, B08404. https://doi.org/10.1029/2011JB008264

Ikari, M. J., Marone, C., Saffer, D. M., & Kopf, A. J. (2013). Slip weakening as a mechanism for slow earthquakes. *Nature Geoscience*, *6*(6), 468–472. https://doi.org/10.1038/ngeo1818

Ikari, M. J., Carpenter, B. M., Vogt, C., & Kopf, A. J. (2016). Elevated time-dependent strengthening rates observed in San Andreas fault drilling samples. *Earth and Planetary Science Letters*, *450*, 164–172. https://doi.org/10.1016/j.epsl.2016.06.036

Kanagawa, K., Cox, S. F., & Zhang, S. (2000). Effects of dissolution–precipitation processes on the strength and mechanical behavior of quartz gouge at high-temperature hydrothermal conditions. *Journal of Geophysical Research*, *105*(B5), 11,115–11,126. https://doi.org/10.1029/2000JB900038

Kaneko, Y., Nielsen, S. B., & Carpenter, B. M. (2016). The onset of laboratory earthquakes explained by nucleating rupture on a rate-and-state fault. *Journal of Geophysical Research: Solid Earth*, *121*, 6071–6091. https://doi.org/10.1002/2016JB013143

Kennely, T. C. (1967). The influence of mineral composition on the residual strength of natural soils. In *Proceedings of the geotechnical conference on shear strength properties of natural soils and rocks, Oslo, Norway* (pp. 123–129). Oslo: Norwegian Geotechnical Institute.

Lapusta, N., & Rice, J. R. (2003). Nucleation and early seismic propagation of small and large events in a crustal earthquake model. *Journal of Geophysical Research*, *108*, 2205. https://doi.org/10.1029/2001JB000793

Lindsay, N. G., Murphy, F. C., Walsh, J. J., & Watterson, J. (1992). Outcrop studies of shale smears on fault surface. In S. S. Flint & I. D. Bryant (Eds.), *The geological modelling of hydrocarbon reservoirs and outcrop analogues* (pp. 113–123). Oxford, UK: Blackwell Publishing Ltd. https://doi.org/10.1002/9781444303957.ch6

Liteanu, E., & Spiers, C. J. (2009). Influence of pore fluid salt content on compaction creep of calcite aggregates in the presence of supercritical CO_2. *Chemical Geology*, *265*(1-2), 134–147. https://doi.org/10.1016/j.chemgeo.2008.12.010

Lockner, D. A., Solum, J. G., & Davatzes, N. (2006). The effect of brine composition and concentration on strength of expandable clays. Abstract T31F-03 presented at the 2006 Fall Meeting, AGU, CA.

Logan, J. M., Friedman, M., Higgs, N., Dengo, C., & Shimamoto, T. (1979). Experimental studies of simulated gouge and their application to studies of natural fault zones, *US Geological survey Open-File Rep.*, 79–1239.

Lüders, V., Plessen, B., Romer, R. L., Weise, S. M., Banks, D. A., Hoth, P., … Schettler, G. (2010). Chemistry and isotopic composition of Rotliegend and Upper Carboniferous formation waters from the North German Basin. *Chemical Geology*, *276*(3-4), 198–208. https://doi.org/10.1016/j.chemgeo.2010.06.006

Majer, E. L., Baria, R., Stark, M., Oates, S., Bommer, J., Smith, B., & Asanuma, H. (2007). Induced seismicity associated with enhanced geothermal systems. *Geothermics*, *36*(3), 185–222. https://doi.org/10.1016/j.geothermics.2007.03.003

Marone, C. J. (1998). Laboratory-derived friction laws and their application to seismic faulting. *Annual Review of Earth and Planetary Sciences*, *26*(1), 643–696. https://doi.org/10.1146/annurev.earth.26.1.643

Miao, C. D., & Fenellif, G. B. (1994). Residual strength of kaolin and bentonite: The influence of their constituent pore fluid. *Geotechnique*, *44*(2), 217–226. https://doi.org/10.1680/geot.1994.44.2.217

Mizoguchi, K., Hirose, T., Shimamoto, T., & Fukuyama, E. (2008). Internal structure and permeability of the Nojima fault, southwest Japan. *Journal of Structural Geology*, *30*(4), 513–524. https://doi.org/10.1016/j.jsg.2007.12.002

Moore, R. (1991). The chemical and mineralogical controls upon the residual strength of pure and natural clays. *Geotechnique*, *41*(1), 35–47. https://doi.org/10.1680/geot.1991.41.1.35

Moore, D. E., & Lockner, D. A. (2004). Crystallographic controls on the frictional behavior of dry and water-saturated sheet structure minerals. *Journal of Geophysical Research*, *109*, B03401. https://doi.org/10.1029/2003JB002582

Moore, D. E., & Lockner, D. A. (2007). Friction of the Smectite clay montmorillonite. In *The seismogenic zone of subduction thrust faults* (pp. 317–345). Columbia University Press. https://doi.org/10.7312/dixo13866-011

Moore, D. E., & Lockner, D. A. (2011). Frictional strengths of talc–serpentine and talc–quartz mixtures. *Journal of Geophysical Research*, *116*, B01403. https://doi.org/10.1029/2010JB007881

Mulders, F. M. M. (2003). *Modelling of stress development and fault slip in and around a producing gas reservoir*. Delft, Netherlands: Delft University of Technology.
NAM (2013). Technical addendum to the Winningsplan Groningen 2013 subsidence, induced earthquakes and seismic hazard analysis in the Groningen field.
Nicol, A., Carne, R., Gerstenberger, M., & Christophersen, A. (2011). Induced seismicity and its implications for CO_2 storage risk. *Energy Procedia*, *4*, 3699–3706. https://doi.org/10.1016/j.egypro.2011.02.302
Niemeijer, A. R., & Collettini, C. (2014). Frictional properties of a low-angle normal fault under in situ conditions: Thermally-activated velocity weakening. *Pure and Applied Geophysics*, *171*(10), 2641–2664. https://doi.org/10.1007/s00024-013-0759-6
Niemeijer, A. R., & Spiers, C. J. (2006). Velocity dependence of strength and healing behaviour in simulated phyllosilicate-bearing fault gouge. *Tectonophysics*, *427*(1-4), 231–253. https://doi.org/10.1016/j.tecto.2006.03.048
Niemeijer, A. R., & Spiers, C. J. (2007). A microphysical model for strong velocity weakening in phyllosilicate-bearing fault gouges. *Journal of Geophysical Research*, *112*, B10405. https://doi.org/10.1029/2007JB005008
Niemeijer, A. R., & Vissers, R. L. M. (2014). Earthquake rupture propagation inferred from the spatial distribution of fault rock frictional properties. *Earth and Planetary Science Letters*, *396*, 154–164. https://doi.org/10.1016/j.epsl.2014.04.010
Niemeijer, A. R., Spiers, C. J., & Peach, C. J. (2008). Frictional behaviour of simulated quartz fault gouges under hydrothermal conditions: Results from ultra-high strain rotary shear experiments. *Tectonophysics*, *460*(1-4), 288–303. https://doi.org/10.1016/j.tecto.2008.09.003
Orlic, B., & Wassing, B. B. T. (2012). Modeling stress development and fault slip in producing hydrocarbon reservoirs overlain by rock salt caprocks., In *46th US Rock Mechanics/Geomechanics Symposium. American Rock Mechanics Association*.
Peach, C. J., & Spiers, C. J. (1996). Influence of crystal plastic deformation on dilatancy and permeability development in synthetic salt rock. *Tectonophysics*, *256*(1-4), 101–128. https://doi.org/10.1016/0040-1951(95)00170-0
Pluymakers, A. M. H., Samuelson, J. E., Niemeijer, A. R., & Spiers, C. J. (2014). Effects of temperature and CO_2 on the frictional behavior of simulated anhydrite fault rock. *Journal of Geophysical Research: Solid Earth*, *119*, 8728–8747. https://doi.org/10.1002/2014JB011575
Pluymakers, A. M. H., Niemeijer, A. R., & Spiers, C. J. (2016). Frictional properties of simulated anhydrite/dolomite fault gouge: Implications for seismogenic potential. *Journal of Structural Geology*, *84*, 31–46. https://doi.org/10.1016/j.jsg.2015.11.008
Pokrovsky, O. S., Golubev, S. V., & Schott, J. (2005). Dissolution kinetics of calcite, dolomite and magnesite at 25°C and 0 to 50 atm pCO2. *Chemical Geology*, *217*(3–4 SPEC. ISS.)(3-4), 239–255. https://doi.org/10.1016/j.chemgeo.2004.12.012
Rice, J. R. (1978). Thermodynamics of the quasi-static growth of Griffith cracks. *Journal of the Mechanics and Physics of Solids*, *26*(2), 61–78. https://doi.org/10.1016/0022-5096(78)90014-5
Ruina, A. (1983). Slip instability and state variable friction laws. *Journal of Geophysical Research*, *88*(B12), 10,359–10,370. https://doi.org/10.1029/JB088iB12p10359
Samuelson, J., & Spiers, C. J. (2012). Fault friction and slip stability not affected by CO_2 storage: Evidence from short-term laboratory experiments on North Sea reservoir sandstones and caprocks. *International Journal of Greenhouse Gas Control*, *11*, S78–S90. https://doi.org/10.1016/j.ijggc.2012.09.018
Scholz, C. H. (1998). Earthquakes and friction laws. *Nature*, *391*(6662), 37–42. https://doi.org/10.1038/34097
Scholz, C. H. (2002). *The mechanics of earthquakes and faulting* (2nd ed.). Cambridge, UK: Cambridge University Press. https://doi.org/10.1017/CBO9780511818516
Scuderi, M. M., Niemeijer, A. R., Collettini, C., & Marone, C. (2013). Frictional properties and slip stability of active faults within carbonate—Evaporite sequences: The role of dolomite and anhydrite. *Earth and Planetary Science Letters*, *369-370*, 220–232. https://doi.org/10.1016/j.epsl.2013.03.024
Segall, P., & Rice, J. R. (2006). Does shear heating of pore fluid contribute to earthquake nucleation? *Journal of Geophysical Research*, *111*, B09316. https://doi.org/10.1029/2005JB004129
Sibson, R. H. (1986). Earthquakes and rock deformation in crustal fault zones. *Annual Review of Earth and Planetary Sciences Letters*, *14*(1), 149–175. https://doi.org/10.1146/annurev.ea.14.050186.001053
Spetzler, J., & Dost, B. (2017). Hypocenter estimation of induced earthquakes in Groningen. *Geophysical Journal International*, *209*(1), 453–465.
Suckale, J. (2010). Moderate-to-large seismicity induced by hydrocarbon production. *The Leading Edge*, *29*(3), 310–319. https://doi.org/10.1190/1.3353728
Takahashi, M., Mizoguchi, K., Kitamura, K., & Masuda, K. (2007). Effects of clay content on the frictional strength and fluid transport property of faults. *Journal of Geophysical Research*, *112*, B08206. https://doi.org/10.1029/2006JB004678
Tembe, S., Lockner, D. A., Solum, J. G., Morrow, C. A., Wong, T. F., & Moore, D. E. (2006). Frictional strength of cuttings and core from SAFOD drillhole phases 1 and 2. *Geophysical Research Letters*, *33*, L23307. https://doi.org/10.1029/2006GL027626
Tembe, S., Lockner, D. A., & Wong, T. F. (2010). Effect of clay content and mineralogy on frictional sliding behavior of simulated gouges: Binary and ternary mixtures of quartz, illite, and montmorillonite. *Journal of Geophysical Research*, *115*, B03416. https://doi.org/10.1029/2009JB006383
Tesei, T., Collettini, C., Carpenter, B. M., Viti, C., & Marone, C. (2012). Frictional strength and healing behavior of phyllosilicate-rich faults. *Journal of Geophysical Research*, *117*, B09402. https://doi.org/10.1029/2012JB009204
Toy, V. G., Boulton, C. J., Sutherland, R., Townend, J., Norris, R. J., Little, T. A., … Carpenter, B. M. (2015). Fault rock lithologies and architecture of the central Alpine fault, New Zealand, revealed by DFDP-1 drilling. *Lithosphere*, *7*(2), 155–173. https://doi.org/10.1130/L395.1
Tullis, T. E. (1993). The effect of pore fluid chemistry on the friction of quartz gouge. In *Proceedings of workshop LXIII, the mechanical involvement of fluids in faulting* (pp. 509–513). Menlo Park, CA: Geological Survey (U.S.) & National Earthquake Hazards Reduction Program (U.S.).
Van Eijs, R. M. H. E., Mulders, F. M. M., Nepveu, M., Kenter, C. J., & Scheffers, B. C. (2006). Correlation between hydrocarbon reservoir properties and induced seismicity in the Netherlands. *Engineering Geology*, *84*(3-4), 99–111. https://doi.org/10.1016/j.enggeo.2006.01.002
van Thienen-Visser, K., & Breunese, J. N. (2015). Induced seismicity of the Groningen gas field: History and recent developments. *The Leading Edge*, *34*(6), 664–671. https://doi.org/10.1190/tle34060664.1
Van Wees, J. D., Buijze, L., van Thienen-visser, K., Nepveu, M., Wassing, B. B. T., Orlic, B., & Fokker, P. A. (2014). Geomechanics response and induced seismicity during gas field depletion in the Netherlands. *Geothermics*, *52*, 206–219. https://doi.org/10.1016/j.geothermics.2014.05.004
Verberne, B. A. (2015). *Strength, stability, and microstructure of simulated calcite faults sheared under laboratory conditions spanning the brittle-plastic transition*. Utrecht, Netherlands: Utrecht University.
Verberne, B. A., He, C., & Spiers, C. J. (2010). Frictional properties of sedimentary rocks and natural fault gouge from the Longmen Shan fault zone, Sichuan, China. *Bulletin of the Seismological Society of America*, *100*(5B), 2767–2790. https://doi.org/10.1785/0120090287

Verberne, B. A., Spiers, C. J., Niemeijer, A. R., de Bresser, J. H. P., de Winter, D. A. M., & Plümper, O. (2013). Frictional properties and microstructure of calcite-rich fault gouges sheared at sub-seismic sliding velocities. *Pure and Applied Geophysics*, *171*(10), 2617–2640. https://doi.org/10.1007/s00024-013-0760-0

Verberne, B. A., Plümper, O., De Winter, D. A. M., & Spiers, C. J. (2014). Superplastic nanofibrous slip zones control seismogenic fault friction. *Science*, *346*(6215), 1342–1344. https://doi.org/10.1126/science.1259003

Walter, L. M. (1986). Relative efficiency of carbonate dissolution and precipitation during diagenesis: A progress report on the role of solution chemistry. *Journal of Sedimentary Petrology*, *56*, 1–11.

Wassing, B., Buijze, L., & Orlic, B. (2017). The impact of visco-elastic caprock on fault reactivation and fault rupture in producing gas fields, *Schatzalp 2nd Induc. Seism. Work*.

Yielding, G., Freeman, B., & Needham, D. T. (1997). Quantitative fault seal prediction 1. *American Association of Petroleum Geologists*, *81*(6), 897–917.

Zhang, Y., & Dawe, R. A. (2000). Influence of Mg^{2+} on the kinetics of calcite precipitation and calcite crystal morphology. *Chemical Geology*, *163*(1-4), 129–138. https://doi.org/10.1016/S0009-2541(99)00097-2

Zhang, L., & He, C. (2013). Frictional properties of natural gouges from Longmenshan fault zone ruptured during the Wenchuan M_w7.9 earthquake. *Tectonophysics*, *594*, 149–164. https://doi.org/10.1016/j.tecto.2013.03.030

Zuddas, P., & Mucci, A. (1994). Kinetics of calcite precipitation from seawater. 1. A classical chemical-kinetics description for strong electrolyte-solutions. *Geochimica et Cosmochimica Acta*, *58*(20), 4353–4362. https://doi.org/10.1016/0016-7037(94)90339-5